



UNIVERSITYTRANSPORTATIONCENTER
FOR UNDERGROUND TRANSPORTATION INFRASTRUCTURE

**SPALL PROTECTION FOR STRUCTURAL TUNNEL LINERS
SUBJECTED TO BLAST OR FIRE**

FINAL PROJECT REPORT

by
Aerik Carlton¹
Ziyan Ouyang¹
Spencer E. Quiel¹
Clay J. Naito¹
¹ Lehigh University

Sponsorship
UTC-UTI

For

University Transportation Center for
Underground Transportation Infrastructure
(UTC-UTI)

February 22, 2020



COLORADOSCHOOL OF MINES
EARTH • ENERGY • ENVIRONMENT



CAL STATE LA
CALIFORNIA STATE UNIVERSITY, LOS ANGELES



Disclaimer

The contents of this report reflect the views of the authors, who are responsible for the facts and the accuracy of the information presented herein. This document is disseminated in the interest of information exchange. The report is funded, partially or entirely, by a grant from the U.S. Department of Transportation's University Transportation Centers Program. However, the U.S. Government assumes no liability for the contents or use thereof.

1. Report No.	2. Government Accession No.	3. Recipient's Catalog No.	
4. Title and Subtitle Spall Protection for Structural Tunnel Liners Subjected to Blast or Fire		5. Report Date February 22, 2020	
		6. Performing Organization Code	
7. Author(s) Carlton, A., Ouyang, Z., Quiel, S.E., and Naito, C.J.		8. Performing Organization Report No.	
9. Performing Organization Name and Address University Transportation Center for Underground Transportation Infrastructure (UTC-UTI) Tier 1 University Transportation Center Colorado School of Mines Coolbaugh 308, 1012 14th St., Golden, CO 80401		10. Work Unit No. (TRAIS)	
		11. Contract or Grant No.	
12. Sponsoring Agency Name and Address United States of America Department of Transportation Research and Innovative Technology Administration		13. Type of Report and Period Covered	
		14. Sponsoring Agency Code	
15. Supplementary Notes Report also available at: https://zenodo.org/communities/utc-uti			
16. Abstract Concrete is prevalently used in modern tunnel construction; however, concrete spall due to extreme fire events and blast diminished the integrity, serviceability and safety. Because of the relatively high requirements on conducting blast-related study and low vulnerability of tunnel liner compared to tunnel drop ceilings, this study concentrates on spall protection for structural tunnel liners subjected to fire. Twenty-four normal weight concrete panel specimens were experimentally subjected to high-intensity single-sided thermal loading (applied via custom gas-fired radiant burner, delivering near ASTM E1529 flux) under constant uniaxial load. The inventory of 150-mm thick panel specimens included three mix designs, two steel reinforcement configurations, and three curing processes. The three mix designs produced compressive strengths of 38, 40, and 47 MPa with nominal cover of 38.1 mm and reinforcement ratios of either 0.006 or 0.008. Two mix designs produced very similar water permeable void ratios (defined by ASTM C642) around 13%, while the third mix expressed 9.2% void by volume. Three levels of axial load were applied at 2%, 16%, and 28% of the nominal concrete compressive strength. Moisture content, internal relative humidity, and ambient temperature were recorded prior to testing. Twenty specimens explosively spalled, while the remainder expressed surface cracking. Specimens with 13% void ratio spalled at 16% or greater axial load, over a wide range of moisture content, ranging 2.4 to 4.6%. When the applied load was reduced to 2% spalling behavior was not observed. The 9.2% void ratio specimens spalled at MC at or above 3.5%, below this threshold however, spalling occurred at lower relative humidity (below 25%) but was avoided at higher relative humidity (above 65%). The results of this study further reinforce the premise that explosive spalling in rapidly heated concrete is influenced by the interaction and summation of thermal stress, pore pressure stress, and mechanical stress from applied load.			
17. Key Words Thermal Concrete Spall, Concrete in Fire, Concrete Behavior at Elevated Temperature		18. Distribution Statement No restrictions.	
19. Security Classification (of this report) Unclassified	20. Security Classification (of this page) Unclassified	21. No of Pages 53	22. Price NA

TABLE OF CONTENTS

Table of Figures	5
List of Tables	6
List of Abbreviations	7
Executive Summary	8
Chapter 1 - Introduction.....	9
Chapter 2 - Background.....	10
2.1 Structural Tunnel Liners Subjected to Fire.....	10
2.2 Structural Tunnel Liners Subjected to Blast	13
Chapter 3 – Experimental Program.....	15
3.1 Concrete Specimens.....	15
3.2 Test Setup.....	22
3.3 Thermal Loading.....	24
3.4 Applied Axial Loading	26
Chapter 4 – Results and Discussion.....	28
4.1 Effects of Heating Time History.....	35
4.2 Effects of Varying Moisture Conditions at Similar Axial Load	40
4.3 Effects of Varying Axial Load at Similar Moisture Conditions	41
4.4 Effects of Varying Heat Flux at Similar Axial Load	43
Chapter 5 – Summary and Conclusions.....	45
References.....	47
Appendix A – Technology Transfer Activities.....	51
Appendix B - Data From the Project	53

TABLE OF FIGURES

Figure 1: Concrete condition at elevated temperature	11
Figure 2: Concrete specimen detail.....	15
Figure 3: SEM 840x magnification concrete mix comparison	19
Figure 4: SEM 6500x magnification concrete mix comparison	19
Figure 5: Moisture content measurement locations	20
Figure 6: Concrete heat and loading frame concept (based on H-TRIS [40])	22
Figure 7: Self-reacting axial and heating load frame.....	23
Figure 8: Heat source configurations (a) concept model (b) actual (c) F1 grill material failure (d) F2 and F3 grill material (e) F2 failure location.....	24
Figure 9: Testing apparatus heat flux calibration setup	25
Figure 10: Calibrated heat flux time history curves including reference to ASTM E1529	26
Figure 11: Total axial load time histories for all specimens	27
Figure 12: RH and VD compared to MC results summary	33
Figure 13: Temperature time histories at 25.4-mm depth embedded thermocouple for (a) all specimens up to 30 minutes of exposure, (b) all specimens up to 12 minutes of exposure, and (c-e) grouped by concrete mix.....	35
Figure 14: Temperature time histories at 25.4-mm depth for (a) all specimens up to 30 minutes of exposure, (b) all specimens up to 12 minutes of exposure, and (c-e) grouped by heating curve .	36
Figure 15: Surface temperature time histories at top of exposed face location (a) all specimens up to 30 minutes of exposure, (b) all specimens up to 12 minutes of exposure, and (c-e) grouped by heating curve	37
Figure 16: Spalled specimens at standard axial load: imparted energy against (a) spall time (b) spall depth at the center of the panel specimen heat exposed area (c) moisture content; and (d) spall depth against moisture content.	38
Figure 17: Temperature time history at 25.4-mm depth for all specimens, color-mapped by (a) moisture content and (b) actual vapor density by raw temperature; (c-e) moisture content and (f-h) vapor density by change in temperature above ambient.....	41
Figure 18: (a) Axial load variation subset 25.4-mm (1-in) embedded thermocouple sensor temperature comparison, (b) C3 all thermocouple sensor temperature time history comparison	42
Figure 19: Heat Flux Variation (a) 25.4 mm depth temperature time history (b) MC to VD	44

LIST OF TABLES

Table 1: Concrete mix summary and comparison	17
Table 2: Cylinder testing summary for concrete age over the experimental testing period	17
Table 3: Void structure and thermal property summary	18
Table 4: Pretesting specimen condition summary	21
Table 5: Summary of heated panel test results	28
Table 6: Post-test perspective-corrected photos of the tested face of each specimen.	30

LIST OF ABBREVIATIONS

CHPP: Center of Highway Pavement Preservation

MDOT: Michigan Department of Transportation

MC: Moisture Content

RH: Relative Humidity

VD: Actual Vapor Density

EXECUTIVE SUMMARY

Concrete is prevalently used in modern tunnel construction; however, concrete spall due to extreme fire events and blast diminished the integrity, serviceability and safety. Because of the relatively high requirements on conducting blast-related study and low vulnerability of tunnel liner compared to tunnel drop ceilings, this study concentrates on spall protection for structural tunnel liners subjected to fire. Twenty-four normal weight concrete panel specimens were experimentally subjected to high-intensity single-sided thermal loading (applied using a custom gas-fired radiant burner, delivering near ASTM E1529 flux) under constant uniaxial load. The inventory of 150-mm thick panel specimens included three normal weight concrete mix designs, two steel reinforcement configurations, and three curing processes. The three mix designs produced compressive strengths of 38, 40, and 47 MPa with nominal cover of 38.1 mm and reinforcement ratios of either 0.006 or 0.008 (achieved using conventional rebar layouts). Two mix designs produced very similar water permeable void ratios (defined by ASTM C642) around 13%, while the third mix had less void with only 9.2%, by volume. Three levels of axial load was applied at approximately to 2%, 16%, and 28% of the nominal concrete compressive strength. Moisture content, internal relative humidity, and ambient temperature were recorded prior to testing. Twenty specimens explosively spalled, with the remainder showing some post-test surface cracking but no explosive behavior. The specimens with the higher 13% void ratio explosively spall over a wide range of moisture contents (ranging from 2.4% to 4.6%) when axially loaded to either 16% or 28% of nominal compressive strength. When the applied load was reduced to 2%, a specimen with a higher void ratio mix and 2.9% by mass moisture content did not spall. Specimens with the lower 9.2% void ratio spall regardless of applied loading at moisture contents above 3.5%. Below that level, explosive spalling occurred at lower relative humidity (below 25%) but was avoided at higher relative humidity (above 65%). The results of this study further reinforce the premise that explosive spalling in rapidly heated concrete is influenced by the interaction and summation of thermal stress, pore pressure stress (influenced by the concrete material's moisture conditions and void ratio), and mechanical stress from the applied load.

CHAPTER 1 - INTRODUCTION

Concrete is widely viewed in structural design as a best-choice fire-resistant material due to its low thermal conductivity and non-combustibility. However, concrete exhibits strength and stiffness losses when subjected to elevated temperatures with strength reductions having been well researched [1–4] with standardized estimates for residual capacity determinations [5]. In addition, concrete under thermal load may exhibit explosive spalling, which currently, does not have a codified design criterion; nor is there an agreed upon methodology for the prediction or mitigation of the behavior.

Blast events in tunnels can be categorized by the quantity of explosive. A large size event caused by a terrorist act or accidental detonation of hazardous material could be quantified as greater than approximately 226 kg (500 lb) of TNT. A smaller size event as a result of an explosion following a vehicle accident and fire is likely to be less than the equivalence of 226 kg of TNT. A blast vulnerability assessment study [6] examined the damage done to tunnel liners as a result of detonation of 226.8 kg (500 lbs), 453.6 kg (1000 lbs) and 907.2 kg (2000 lbs) of TNT. The study found that under these demands the tunnel liner is subject to near field blast effects and is likely to exhibit localized spall and breach. A typical concrete tunnel liner was shown to locally initiate damage at charge sizes of 226.8 kg (500 lbs) of TNT and exhibit significant regional damage at higher explosive sizes.

Concrete spalling is defined as fragment detachment from an exposed surface, which has been observed, under heating, to violently explode or to exhibit progressive material peeling [7–9]. Spalling results in loss of section, and in extreme cases has been observed to breach the entire structural thickness [10]; increasing the possibility of progressive failures. Loss of section can expose steel reinforcement resulting in premature strength degradation and loss of flexural capacity for reinforced concrete structural elements due to the significant reduction in steel strength at elevated temperatures [11,12].

This report will present a novel fire test method, derived from Maluk et al. (2016), which imposes a controlled radiant heat flux time-history on a concrete sample as a departure from the conventional standard furnace testing; specifically aimed at concrete spalling behavior observation. Experimentation was designed around the reduction of difference between real structure and test specimen behavior; specifically using specimen thicknesses nearing typical structural element thickness, and the inclusion of axial load. Compressive loads representing typical in-service conditions were applied prior and during heat exposure. Most of the existing experimental record regarding thermally induced concrete spalling, as well as analytical prediction, have relied on concrete cylinder specimens without loading/restraining stress [14,15]. The experimental results contained herein, suggests pore vapor pressure plays a significant, if not controlling, role in the occurrence of spall, as initial moisture condition, thermal behavior, and loading conditions do not present a clear demarcation for spall occurrence.

CHAPTER 2 - BACKGROUND

2.1 Structural Tunnel Liners Subjected to Fire

Approaching the problem of explosive concrete spalling due to thermal exposure, several material properties which change at elevated temperatures must be considered: thermal conductivity, moisture condition, and void structure. During heating, the material temperature has been shown to propagate through thickness contingent upon the material's thermal conductivity [16]. Thermal conductivity is effected by several factors: the amount and type of cement, the types of admixtures, aggregate to cement fraction, temperature, and moisture state [17]; however codified standard equations as functions of temperature have been established [18] and typically show good agreement with physical testing.

Concrete moisture condition can be described by several metrics, typically: Moisture Content (MC), Relative Humidity (RH), and/or actual Vapor Density (VD). MC is a percentage by mass of the water present in the sample. RH is a percentage of the saturated vapor density, quantifying the gaseous water normalized by the saturated vapor density. Where, saturated vapor density is a function of temperature, in this instance the ambient temperature of the concrete. VD is the density of water vapor in the material in grams per cubic meter. The MC is typically considered the metric for liquid water in concrete, as water vapor consists of such a small portion of the overall mass that the effects of vapor to measured MC by mass is negligible [19]. RH and VD are directly related, reporting the same information about the gaseous water within a sample. However, RH is normalized by temperature via the saturated vapor pressure requiring an ambient material temperature to as be reported to fully define the vapor state, whereas VD reports the direct quantity of vapor without normalization. Most researchers evaluating concrete under fire, report the MC or the RH. Rarely are both MC and RH/VD values reported for the initial moisture state. MC, RH, and a calculated actual Vapor Density (VD) are presented in this paper, because MC to VD result comparisons showed a greater spread in the tested samples moisture condition definition than the MC to RH comparison and suggest a demarcation for spall occurrence.

Figure 1 illustrates the concept of thermal conductivity, moisture condition, and void structure in the context of concrete heating one-dimensionally, while also introducing the concept of the “moisture clog;” coined in the 1960s by Shorter and Harmathy [20,21]. The “void” shown in the upper right of Figure 1 illustrates a void partially filled with liquid water and water vapor. MC and RH/VD are related but not interchangeably, as the ambient material temperature, moisture history (i.e. curing method and saturation cycling history), and capillary condensation conditions effect the RH range allowed by the available water at a specific MC [22,23]. RH/VD changes more quickly than MC [19] as gas permeability is typically two orders of magnitude greater than liquid permeability in concrete [22]. Additionally, RH/VD is much more sensitive to the ambient temperature than MC [19]. The arrows around the “void” in Figure 1 are meant to represent the movement of either gas or liquid in relative relationship to the associated rate of permeability of that phase.

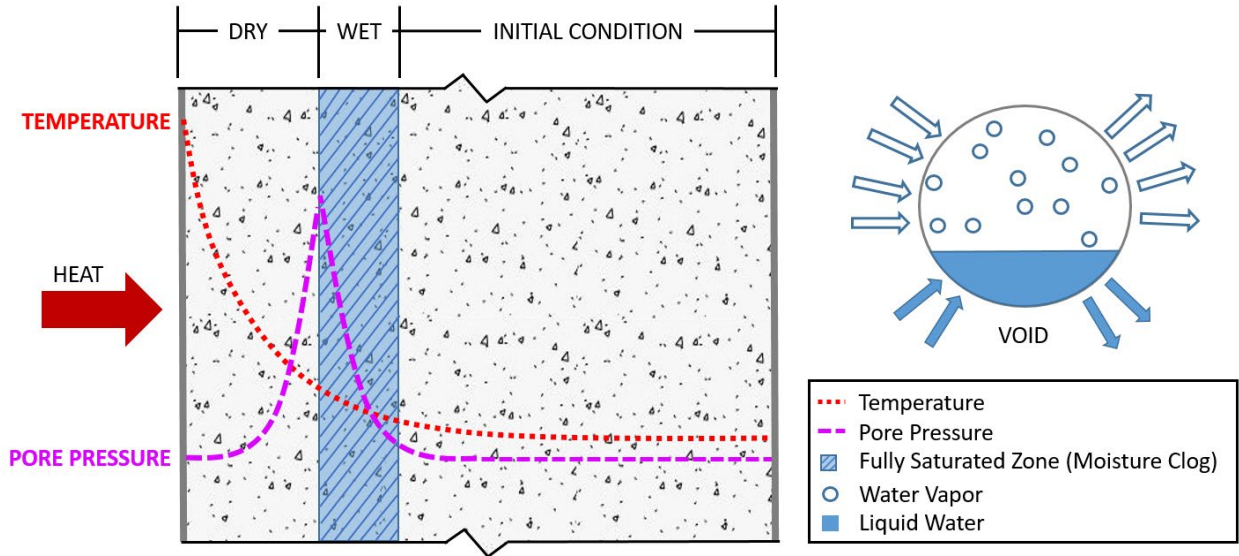


Figure 1: Concrete condition at elevated temperature

The behavior of concrete at elevated temperatures is complex, and includes changes in permeability, pore pressure, constituent phase, thermal conductivity, strength, and void structure [7,14,20,24]. Some properties are reversible under certain conditions, but irreversible under others. For example, gas permeability is effected by the moisture condition of the specimen and changes reversibly between moisture conditions (however, gas permeability is effected by moisture condition history [22]), yet gas permeability changes become irreversible when temperatures exceed material strengths. Adequate accounting of the moisture condition through time is requisite when describing and predicting thermally-induced explosive concrete spalling.

Void structure is used, herein, to envelop the concepts of void percentage and void connectivity (e.g., gas permeability, water permeability, absorption, and the associated rates of permeability). ASTM C642, ASTM C1757, and Scanning Electron Microscopy (SEM) images were all recorded in this paper to aid in the description of the void structure [25,26]. An increase in pore pressure occurs with the increase in temperature, so long as there is available liquid water to feed the increasing vapor density while maintaining the void structure. If the voids are compromised by exceeding the material strength limits of the concrete, cracking can occur which will relieve pore pressure by providing ventilation routes for the built-up vapor. The concept of vapor venting is supported by spall mitigation experimentation of polypropylene fiber concrete mix designs [27–29].

Figure 1 shows a representative concrete specimen in one dimension; a plane through the structural thickness. As heat is applied to the page-left surface of the specimen, a temperature gradient (shown with a red dotted-line) consistent with exponential decay from the surface temperature to the ambient concrete temperature is typical. Pore pressures are low at the heat exposed surface, even though material temperature is highest, because venting routes are clear of liquid, allowing vapor to vent. At later heating stages, cracking occurs at high concrete temperatures that increase vapor venting.

The moisture clog occurs as the vapor permeating into the structural thickness, away from the heated surface, reaches cooler material temperatures, allowing for condensation. The condensed vapor increases the existing liquid water present in the voids. When the voids approach the fully saturated state, pore pressure buildup is observed at the boundary between the saturated and dry concrete layers [20,24], thus the clog condition. Figure 1 denotes the fully-saturated zone as the blue hashed area. The moisture clog is a moving front due to the changes to material temperature and permeability. Where the convergence of increasing temperatures phase change fully-saturated layer liquid to vapor while the vapor is constrained by permeability limits, a spalling condition is theorized to occur when stresses exceed material strength.

At the demarcation between the dried and the wet concrete, peak pore pressures have been experimentally observed [7,14,24]. Figure 1 shows the typical behavior of pore pressures during heating (the purple dashed line) with resting state pressures rising to a peak at the dry to saturated boundary. A depth range from heated surface of the drying front can be estimated by the internal material temperature gradient, requiring a minimum of 100°C and a suggested maximum of 400°C [30], however these boundaries are contingent upon pore pressure. As pressure increases the boiling point of water increases proportionally.

Thermomechanical processes and thermos-hygral processes (including chemical dehydration) have been suggested as possible spalling mechanism routes, either individually or in concert [7,14,24]. In the more esoteric, Boiling Liquid Expanding Vapor Explosion (BLEVE) phenomena has also been suggested as a possible spalling mechanism under certain conditions [14]. A 3D differential equation based analytical method has been developed, that has shown accurate time of spall predictions, but lacks methodology for predicting the occurrence or depth of spall [15,31].

Most thermally-induced explosive concrete spalling research has magnified the role of moisture, particularly vapor [15,24,31,32]. Pore pressure behavior, as previously presented in this section, has been found experimentally repeatable and consistent [7,14,24]. However, accurate measurement of internal concrete changes during heat testing has been found to be difficult, especially internal vapor pressure, with most researchers acknowledging difficulty in calibration and/or confidence in measurement precision from embedded pore pressure gauges [7,14,24]. Due to the issues in precision/calibration, cost, and confidence in not skewing spall phenomena due to the introduction of ventilation routes for vapor from embedded pore pressure gauges, the experimentation presented herein did not attempt to measure active pore pressures during heat exposure.

Summarily, thermally-induced explosive concrete spalling does not have an agreed upon method for prediction, due in large part to the variation in results from ranging experimentation methods and the complexity of the behavior. The purpose of this paper is to establish the author's experimental capability to induce explosive thermal concrete spalling behavior, and to comment on the initial experimental results in the context of the limited current codified standards for spall and research record.

2.2 Structural Tunnel Liners Subjected to Blast

Tunnels are particularly vulnerable to terrorist attack since most have uncontrolled public access to vehicles ranging from motorbikes and passenger cars to large cargo-hauling trucks. Though the risk of terrorist attack is low, consideration of these threats is amplified since (1) they typically carry high consequence; (2) they are attracted to high-impact, high-visibility targets, particularly those with lower levels of perceived security; and (3) public fear or dread of these events contributes to “probability neglect,” which is the goal of most terrorist activities (Stewart et al. 2006). Between 1970 and 2015, the United States alone has seen 89 terrorist attacks targeting the transportation sector, 64% of which were carried out through bombings (Miller 2016). Tunnels specifically may pose an even greater concern when considering the additional confinement during a blast as well as the enclosed space in which to operate rescue and repair efforts. Though many recent incidents around the world have involved hand-carried threats in subway tunnels (CNN 2017), US government agencies have been focusing their mitigation efforts more on the threat posed by vehicle-borne improvised explosive devices (VBIEDs) (Transportation Research Board 2006).

The aforementioned NCHRP effort has highlighted a need for improved assessment of transportation tunnel vulnerability to blast (Transportation Research Board 2006). In particular, few available approaches can provide reasonably conservative, computationally efficient evaluations of the spatial distribution and structural consequences of blast-induced damage. Numerous research studies have examined the propagation of blast-induced pressure loads in tunnels and other confined structures via experiments (Edri et al. 2011) (Stolz and Ruiz-Ripoll 2016) and high-fidelity computational fluid dynamic analysis (Feldgun et al. 2008) (Pennetier et al. 2015) (Uystepuyst and Monnoyer 2014). The results of these studies have made strides in establishing the temporal and spatial distribution of blast pressure on tunnel liners. Some studies have used finite element (FE) analyses to model the spalling and/or breach effects of these blast loads on the tunnel liners, which are typically constructed of reinforced concrete (Stolz and Ruiz-Ripoll 2016) (Choi et al. 2006) (Buonsanti and Leonardi 2013). Previous studies have collectively demonstrated that shock-induced cracking, spalling, and breach is the dominant failure mode of tunnel liners in response to blast pressure, as opposed to the flexural response that are more typical of many building or bridge structures.

The most significant contributions made by previous research in this field have typically pertained to the use of high-fidelity modeling tools, which are computationally demanding and are not conducive to parametric assessment of tunnels subjected to blast loads. This report addresses the need for assessment tools of “intermediate” complexity, which can deliver accurate, conservative assessments of blast-induced damage at a fraction of the computational effort of high-fidelity models. A similar approach to intermediate models has been developed previously by one of the authors for the vulnerability of bridges to unconfined hydrocarbon fires (Quiel et al. 2015b). This report will focus on the levels of spall and breach damage induced by VBIED hazards that are traveling in typical roadway tunnels. Three tunnel prototypes with varying geometry but identical vehicle throughput were evaluated for a range of blast hazards. Spatial contours of damage were

developed using the proposed approach and compared well to results obtained from high-fidelity computational analysis.

The approach was used to efficiently establish the relationship between blast hazard intensity and the extent of damage for a range of tunnel design parameters or conditions. The extent of tunnel damage can then be used as the initial conditions for progressive collapse assessment of the tunnel liner. The results indicated that spall of soil backed tunnel liners (the most common transportation system) is limited to the extrados face of the system and is only prevalent in very large explosions. The size of the detonation would need to be much larger than typical accidental events such as a BLEVE event from transport of a conventional HAZMAT gas. In addition, the extrados spall can be minimized if the backing material is of similar stiffness to the liner segment. This is common in bedrock bored tunnels and for cases where a high strength grout is used behind the liner. The issue of blast induced spall damage of the tunnel liner is not a significant concern in these applications.

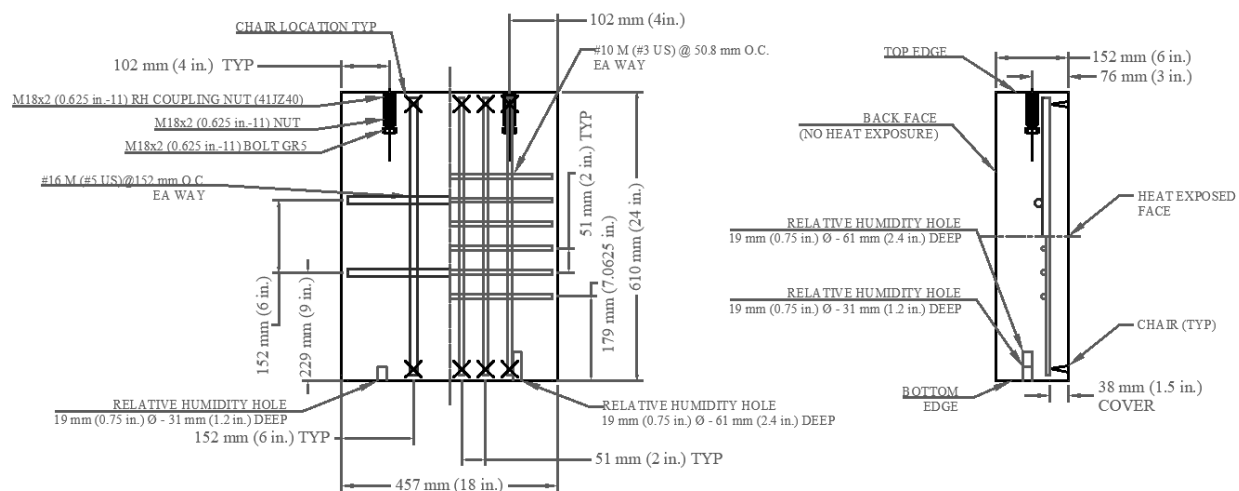
An area of concern was identified in the liner performance was identified in the use of drop ceilings. This component of tunnels acts in a flexural mode and are highly susceptible to failure under very small explosive events. In a subproject funded by a Pennsylvania state agency, the PIs have been evaluating false ceiling structures that are commonly installed in tunnels to separate the main shaft from ventilation and other mechanical systems. Based on the state of knowledge the subsequent experimental program was focused on fire associated spall. Blast induced spalling was found not to be a concern.

CHAPTER 3 – EXPERIMENTAL PROGRAM

The experimental program is first introduced with a detailed description of the test study concrete specimens followed by the testing apparatus and procedure descriptions. Sixty concrete specimens were cast including: 3 used for coring samples, 14 used in experimental apparatus calibration and setup, and 24 fully-tested with in-situ moisture content (MC) percentage by mass and relative humidity (RH) percentages reported shortly before testing. Twenty-four tested specimens include three concrete mix designs, two steel reinforcement configurations, and three curing processes. The three mixes produced compressive strengths of 38, 40, and 47 MPa with nominal cover of 38.1 mm and reinforcement ratios of either 0.006 or 0.008 (achieved using conventional rebar layouts). The experimental program, results, and discussion is focused on the 24 tested specimens. A brief discussion concerning experimental initiation is included in the Results and Discussion section to address subjective elements of the spalling behavior.

3.1 Concrete Specimens

The typical concrete specimen was constructed as shown in Figure 2: 152 mm (6 in.) in thickness, 457 mm (18 in.) in width, and 610 mm (24 in.) in height; with two lifting lugs placed in the top edge to facilitate movement of the sample into and out of the loading frame; and two post-cure drilled relative humidity holes in the bottom edge of each specimen. Figure 2 shows two different reinforcing details in a split specimen format. The first reinforcing configuration includes #16M (#5 US) 420 MPa (Grade 60) steel reinforcing bars arranged with two longitudinal and two transverse, while the second reinforcing configuration includes #10M (#3 US) 420 MPa (Grade 60) steel reinforcing bars arranged with six longitudinal and six transverse. Both reinforcing configurations are located with the same 38 mm (1.5 in.) clear cover between the heat-exposed face and closest steel reinforcing.



Important to note, the heat exposed specimen face is covered at the top and bottom by 83 mm (3.25 in) of the loading frame flanges, which reduces the directly heat exposed area to 2032 mm² (315 in²), minimizing any thermal effects caused by the locations of lifting lug and reinforcing bar location chairs.

For C1 and C2 specimens, three k-type thermocouple sensors were embedded at the center of the width and height; spaced at 25.4 mm (1 in) on center from each other in the width direction; and located at 25.4 mm (1 in), 76.2 mm (3 in), and 127 mm (5 in) from the heated face. C3 specimens had four k-type thermocouple sensors embedded at the center of the width and height; spaced at 25.4 mm (1 in) on center from each other in the width direction; and located at 0 mm (0 in), 6.4 mm (0.25 in), 12.7 mm (0.5 in), and 25.4 mm (1 in) from the heated face. C3 specimens were cast post experimentation of the full C1 and C2 specimen sets, where it was determined that spalling was occurring within 38 mm (1.5 in), to obtain more detailed temperature records of the material within the spalling zone the differing embedded thermocouple locations was used.

Three concrete mix designs: C1, C2, and C3, were examined and are summarized in Table 1. C1 was provided by a commercial precast manufacturer and two batches were used to complete the C1 specimen casting. A slight deviation due to scale tolerance and mix water quantity between C1 batches is shown by ranges in Table 1. C2 and C3 were provided by a commercial concrete supplier and cast in-house. All three mixes sourced the large aggregates (A57 and A8) from the same material supplier from the same or neighboring quarries, with fine aggregate (sand) from the same material supplier and same quarry. Both concrete mix designs were consistent with Pennsylvania Department of Transportation (PennDOT) approved AAA-S3 precast mix design. Noted differences between C1 and C2 are the cement type, pozzolan, inclusion or omission of A8 coarse aggregate, and the admixtures. C3 is similar to C2 but omits the A8 coarse aggregate. Slump and air content were not measured at casting for C2.

Table 1: Concrete mix summary and comparison

Concrete Mix		C1	C2	C3
Cement	Type	III	I	I
	[kg/m ³]	342.5-344.1	245.2	223.5
Pozzolan	Type	Fly Ash	GGBFS	GGBFS
	[kg/m ³]	63.3-67.2	130.5	118.6
Mix Water	[kg/m ³]	108.9-102.3	107.2	95.4
W/C		0.374-0.395	0.399	0.421
Coarse Aggregate	Type	A57	A57	A57
	[kg/m ³]	1022.02-1022.8	609.1	1056
	Type	A8	A8	A8
	[kg/m ³]	None	411.3	None
Fine Aggregate	Type	Sand	Sand	Sand
	[kg/m ³]	785.5-788.7	798.9	822.7
Admixtures	AEA	Darex II	Darex II	Darvair 1000
	[mL/m ³]	206	619	553
	HRWR	ADVA Cast 585	EXP 950	EXP 950
	[mL/m ³]	1083	516	437
	MRWR	None	Daracem 55	Daracem 55
	[mL/m ³]	0	877	437
	RE	None	Daratard 17	Daratard 17
	[mL/m ³]	0	387	669
Measured at Casting	Type	Unit Weight	Unit Weight	Unit Weight
	[kg/m ³]	2338.7	2338.7	2335.5
	Type	Slump	Slump	Slump
	[mm]	172	152 target	178
	Type	Air	Air	Air
	[%]	5	6 target	4.4

Table 2 summarizes the cylinder testing results for the different concrete mix designs. Concrete cylinders of 102 mm diameter by 203 mm of length (4-in dia. by 8-in length) were made and tested in accordance with ASTM C39, C469, and C496 [33–35]. Cylinder results were consistent at same day evaluations. C1 resulted in a higher compressive strength than C2 and C3 as was expected due to the water to cement ratios, however C2 resulted in a slightly higher splitting tension strength than C1 and C3 due to the mixed coarse aggregate gradation. Twenty-eight day strength was not evaluated for C2.

Table 2: Cylinder testing summary for concrete age over the experimental testing period

C1			C2			C3		
Age [days]	Prop.	Value	Age [days]	Prop.	Value	Age [days]	Prop.	Value
581 to 709	Comp.	47.2 ± 1.2 MPa	463 to 573	Comp.	40.0 ± 1.4 MPa	28 to 72	Comp.	38.20 ± 1.8 MPa
	Tens.	4.3 ± 0.1 MPa		Tens.	4.7 ± 0.3 MPa		Tens.	4.2 ± 0.5 MPa
	Mod.	40.2 ± 2.3 GPa		Mod.	35.3 ± 1.2 GPa		Mod.	40.4 ± 4.0 GPa

ASTM C642 and C1757 were completed for each mix to quantify void percentage, density, absorption, and water sorption [25] [26]. Where the void is percentage by volume; absorption is a measure of the solid concrete ability to taken in liquid water; and sorption is another measure of concrete ability to take in water. Sorption, which includes absorption, but also includes the adherence of liquid water to the solid's surface (i.e., adsorption) and ion exchange liquid water uptake. The results of ASTM C642 and C1757 are summarized in Table 3. On average the difference in the void percentage, density, absorption, and sorption as defined by the ASTM standards was approximately 40% between the C1 and both C2 and C3 concrete mixes. C2 and C3 exhibited similar properties and had the larger void percentage, lower bulk/apparent density, and were determined to be more permeable than C1.

A Hot Disk TPS 2500 (which meets the requirements of the ISO 22007-2 standard for thermal conductivity and diffusivity) was used on a series of samples cut from ASTM C39 conforming concrete cylinders for each concrete mix. The ambient temperature values were evaluated for the thermal conductivity, thermal diffusivity, and specific heat for each mix and the average of each value within each concrete mix sample set is reported in Table 3. The thermal conductivity between C2 and C3 is the same, while C1 was less thermally conductive. C2 and C3 differ however in thermal diffusivity and specific heat, however the samples from C3 were of relatively much younger age compared to the C1 and C2 samples and also had different moisture conditions due to a shorter holding period post cutting from cylinders which are likely to be expressed in the thermal diffusivity and specific heat values (as seen between the C2 and C3 diffusivity and specific heat values).

Table 3: Void structure and thermal property summary

Standard	Property	C1	C2	C3
ASTM C642	Absorption after immersion	3.88%	4.92%	5.01%
	Absorption after immersion and boiling	3.88%	5.74%	5.52%
	Volume of permeable pore space (voids)	9.2%	13.0%	13.1%
ASTM C1757	Sorption	0.28 mm	0.39 mm	0.40 mm
ISO 22007-2	Thermal Conductivity	2.76 W/mK	2.82 W/mK	2.82 W/mK
	Thermal Diffusivity	1.65 mm ² /s	1.44 mm ² /s	1.69 mm ² /s
	Specific Heat	1.68 MJ/m ³ K	1.99 MJ/m ³ K	1.67 MJ/m ³ K

In addition to the standards testing in Table 3, SEM was included as a visual confirmation of the mix design differences, and the comparisons are shown in Figure 3 and Figure 4 with C1 shown in (a), C2 in (b), and C3 in (c). The age of the concrete specimens shown in SEM is C1 at 742 days, C2 at 605 days, and C3 at 129 days. C1 was noticeably denser with larger voids widely spaced, while C2 exhibited smaller, more closely spaced voids. The apparent density difference visible in the SEM confirms expectations that higher compressive strength mixes with high thermal conductivity, lower void percentage, and lower permeability would show a denser microstructure; while lower compressive strength mixes with lower thermal conductivity, higher void percentage, and higher permeability would show more frequent, smaller, and more closely spaced voids [17]. The SEM of C1 shows well defined ettringite formation and smooth spherical fly ash particles, while C2 and C3 show a higher proportion of CH crystalline structures and jagged granulated blast

furnace slag. C2 and C3 are very similar mix designs, with only large aggregate (A8) and air entrainment agent (AEA) differences.

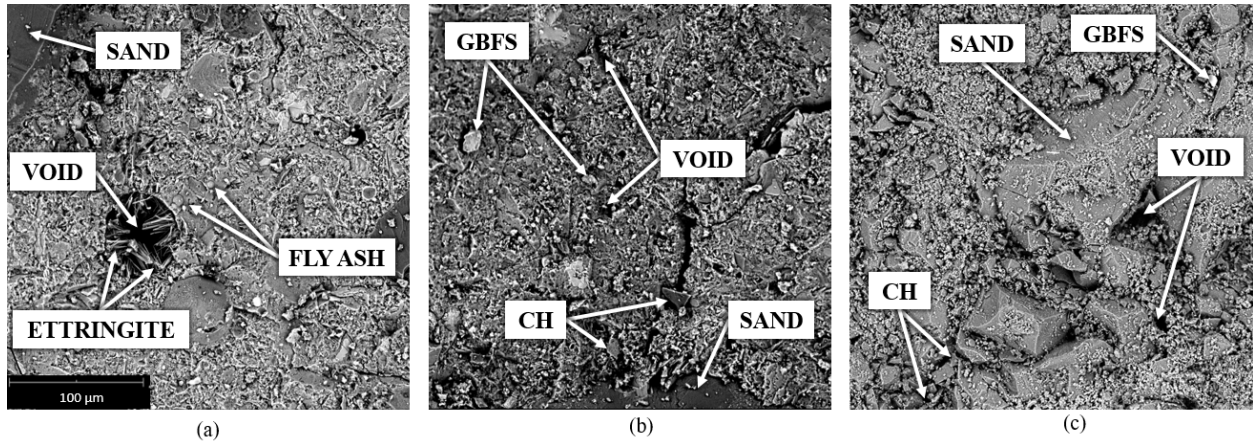


Figure 3: SEM 840x magnification concrete mix comparison

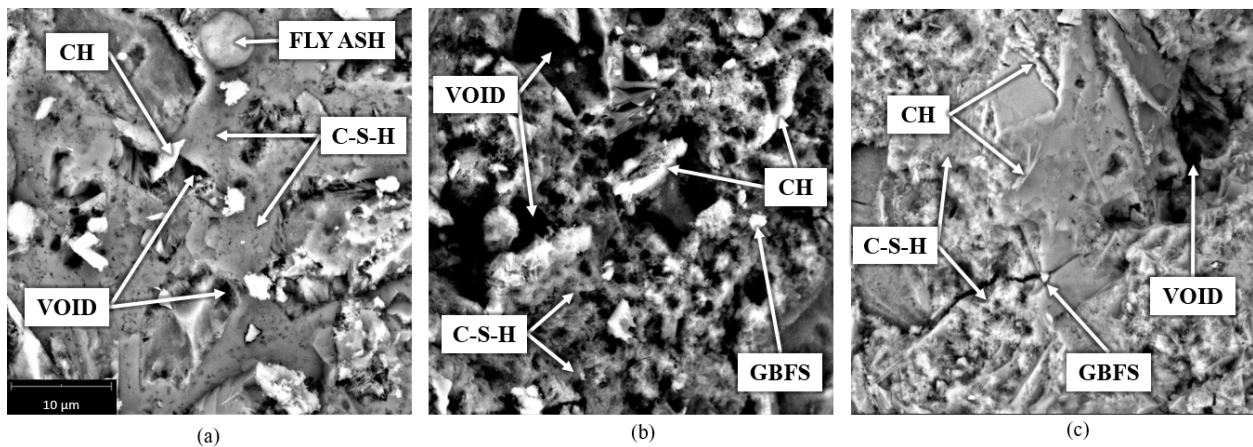


Figure 4: SEM 6500x magnification concrete mix comparison

Concrete moisture readings were taken using a Tramex CMEX II Digital Moisture meter. The meter allows measurement of both MC, via surface contact pins, and RH via an add-on hygrometer probe, inserted into pre-drilled, sleeved, and capped holes. RH holes were drilled using a 19 mm (0.75 in) diameter hammer drill bit, cleaned of debris by vacuum, sleeved, and capped (per meter manufacturer specifications in accordance with ASTM F2170) [36]. Holes were drilled in the bottom edge of each specimen at 31 mm (1.2 in) consistent with ASTM F2170; 20% of thickness for 2-sided drying. After a minimum 24 hour post drilling wait, the Tramex Hygro-i2 relative humidity probe was inserted and sealed into the hole allowing 30 minutes of equilibration time before RH measurement; per specification, an additional RH measurement was taken 5 minutes after the first as a verification procedure, with less than 1% difference between initial and secondary measurement indicating a valid reading. In addition to the RH, the meter hygrometer probe reports ambient material temperature. Using the recorded ambient material temperature and

the saturated vapor density computations defined by the International Association for the Properties of Water and Steam the actual vapor density was determined [37]. Tramex CMEX II meters are calibrated by the manufacturer, and then calibration-verified by a third party ISO/IEC standard 17025 certified laboratory. This type of moisture meter allows for continuous and nondestructive moisture content and relative humidity monitoring.

Specimen MC was periodically monitored for all specimens to allow for test execution at specific moisture conditions. The MC was taken from nine location on the to-be heat exposed face as shown in Figure 5 and averaged. The MC meter estimates the MC for the first 19 mm (0.75 in) of depth which is comparable to the observed spall depths. MC, RH, and material temperature measurements were taken prior to heat exposure testing.

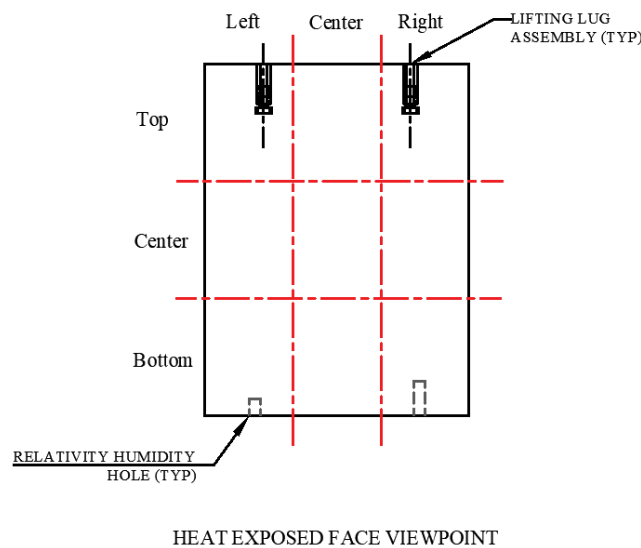


Figure 5: Moisture content measurement locations

Table 4 summarizes the pretest specimen conditions. Each specimen was labeled with the concrete mix, moisture content (MC), actual vapor density (VD), and the applied heat flux curve (e.g., C1-4.1-15.6-F1, represents a specimen from the first concrete mix design, C1, at 4.1% moisture content with 15.6 g/m³ actual vapor density that was tested under the F1 heat flux curve from Figure 10). Typical specimens were air cured (Air), one specimen was water bath (WB) cured for 1 year, and several more specimens were air cured then wet burlap wrapped (Air-BS) and covered with plastic to increase MC, so that a larger range in moisture conditions could be tested.

Table 4: Pretesting specimen condition summary

Label	Test Age	Curing Process	Reinforcing Detail	MC	Air Temp.	Material Temp.	Sat. Vapor Density	RH	VD
	[day]			[%]	[°C]	[°C]	[g/m ³]	31 mm depth [%]	31 mm depth [g/m ³]
C1-4.1-15.6-F1	582	WB	#16M (#5 US)	4.1	27	26.5	23.6	66	15.6
C1-4.1-09.0-F1	650	Air	#16M (#5 US)	4.1	22	22.2	18.8	48	9.0
C1-4.1-08.6-F2	676	Air	#16M (#5 US)	4.1	21	21.4	18.0	48	8.6
C1-3.8-13.2-F1	585	Air	#16M (#5 US)	3.8	27	28.0	23.6	56	13.2
C1-3.8-12.4-F1	595	Air	#16M (#5 US)	3.8	26	26.5	22.5	55	12.4
C1-3.3-16.7-F1	592	Air	#16M (#5 US)	3.3	29	29.4	26.1	64	16.7
C1-3.3-03.4-F3	709	Air	#16M (#5 US)	3.3	17	17.8	15.3	22	3.4
C1-3.0-13.7-F1	593	Air	#16M (#5 US)	3.0	26	26.6	22.5	61	13.7
C2-4.6-18.5-F1	463	Air-BS	#16M (#5 US)	4.6	29	29.0	26.1	71	18.5
C2-4.2-14.9-F1	470	Air-BS	#16M (#5 US)	4.2	27	27.5	23.6	63	14.9
C2-3.9-15.4-F1	469	Air-BS	#16M (#5 US)	3.9	27	27.8	23.6	65	15.4
C2-3.9-10.8-F1	476	Air	#16M (#5 US)	3.9	26	26.3	22.5	48	10.8
C2-3.6-10.1-F1	490	Air	#16M (#5 US)	3.6	22	X	18.8	54	10.1
C2-3.3-07.4-F2	540	Air-BS	#16M (#5 US)	3.3	20	20.3	17.3	43	7.4
C2-3.2-07.4-F2	540	Air-BS	#16M (#5 US)	3.2	20	20.9	17.3	43	7.4
C2-2.9-05.5-F3	571	Air	#16M (#5 US)	2.9	19	20.3	16.6	33	5.5
C2-2.8-04.6-F3	572	Air-BS	#16M (#5 US)	2.8	17	17.6	15.3	30	4.6
C2-2.4-06.7-F3	566	Air	#10M (#3 US)	2.4	17	17.7	15.3	44	6.7
C2-2.4-05.5-F3	572	Air	#10M (#3 US)	2.4	20	20.2	17.3	32	5.5
C2-2.4-03.2-F3	564	Air	#10M (#3 US)	2.4	4.5	22.3	9.0	35	3.2
C3-3.4-13.3-F3	65	Air	#16M (#5 US)	3.4	23	24.0	19.6	68	13.3
C3-3.3-13.3-F3	65	Air	#16M (#5 US)	3.3	23	23.6	19.6	68	13.3
C3-3.0-13.1-F3	72	Air	#16M (#5 US)	3.0	24	X	20.5	64	13.1
C3-2.9-13.6-F3	72	Air	#16M (#5 US)	2.9	24	25.7	20.5	66	13.6

Label: CX (Concrete Mix) - X.X (Moisture Content %) - XX.X (Actual Vapor Density g/m³ at 31 mm depth) - FX (Applied Heat Flux Curve)

WB = Water Bath Cure, **Air** = Air Cure, **Air-BS** = Air Cure with wet Burlap Soaking to increase MC pretest

3.2 Test Setup

The testing apparatus is based upon the experimental setup described in Maluk et al. (2016), consisting of a self-reacting loading frame and heating source mounted on a movable track to control heat flux delivery as shown in Figure 6. A self-reacting load frame with two through-hole hydraulic actuators delivered axial load to the concrete specimen with the heating source mounted on a separate track. The testing apparatus was designed to allow for variation in applied axial load in one-direction while providing variation in applied thermal loading via standoff distance between the heat source and specimen.

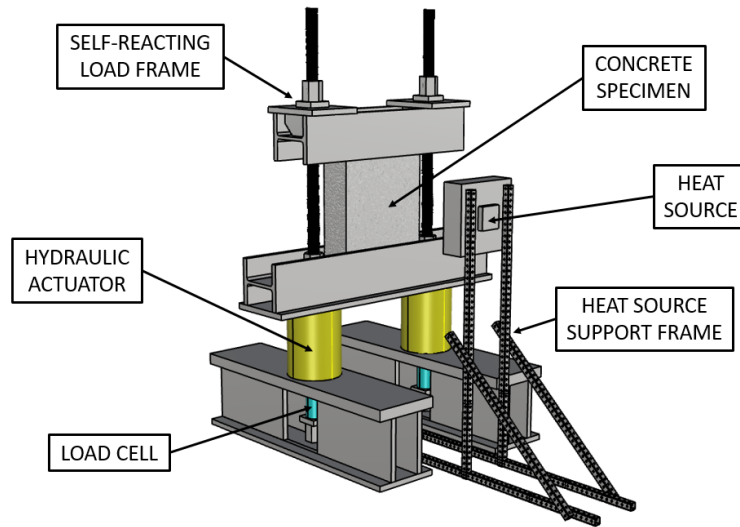


Figure 6: Concrete heat and loading frame concept (based on H-TRIS [13])

The self-reacting frame consists of two double webbed, built-up I-sections acting as spreader beams to distribute the loading frame and specimen weight over a larger floor area. Between the spreader beams dual webs, an opening was cut to facilitate access to, and placement of, the capping nut and washers for the threaded rod and load cells. The threaded rod's bottom nut and washer sandwiches the hollow pipe-style load cell between the washer and the bottom of the spreader beam's top flange. The threaded rod passes through a hollow section hydraulic actuator ram and through a welded plate and w-section that acts as the base support for the concrete specimen. The threaded rods pass the sides of the concrete specimen and through the top built-up plate and wide flange section that acts as the top support for the concrete specimen, and are capped at the top with a nut and washer. The configuration allows for the hydraulic rams to push the bottom specimen support beam upward compressing the concrete sample against the top support beam.

The hydraulic actuators are controlled via a pressure regulated hydraulic fluid pump. The in-line load cells are used to set the delivered axial load as well as monitor the variation in the applied load throughout the heat exposure duration. Axial load of 600 kips can be applied, easily accommodating 30% of the compressive strength of the concrete. Due to the pressure control system the axial load variation is typically within 4% of the targeted value throughout the duration of heat exposure, and also varies 4% between left and right actuators.

The heat source support frame allows for three-dimensional adjustment of the heat source. A sled and track system, which allows movement of the heat source in the direction normal to the exposed specimen surface, was integrated into the heat source support frame. Rapid standoff closing was needed to reduce the effect of heat source ignition on the sample before the initiation of the calibrated heat flux curve, while also adding an element of safety during ignition with increases standoff between specimen and heater.

Figure 7 shows the realized axial and heat loading frame; note the inclusion of insulation wrapping for the heat exposed threaded rod and the hydraulic actuator rams, a spall fragment protection screen, and labeling showing thermocouple sensors. The spall fragment protection screen was constructed of a welded carbon steel angle frame with two layers of stainless steel welded wire mesh bolted in-place at 101.6 mm (4 in) bolt to bolt spacing around the steel angle frame perimeter. The stainless steel mesh layers were replaced every 40 minutes of heat exposure. Several heat exposure cycle iterations were evaluated during heat flux calibration to set the mesh replacement schedule such that the presented heat flux curves were minimally affected by screen condition. The protection screen does impede heat flux delivery to the specimen surface, however all calibration curves presented were recorded with the screen in place (heat flux calibration is discussed in more depth in the next section). Three to four thermocouple sensors were embedded within the concrete specimens at staggered distances from the heat exposed specimen face. Additionally, two thermocouple sensors were placed in contact with the specimen at the top and bottom of the heat exposed area, located on center of the specimen width, between the spall protection screen and specimen. The surface temperatures reported, herein, are the top and bottom surface measurements average.

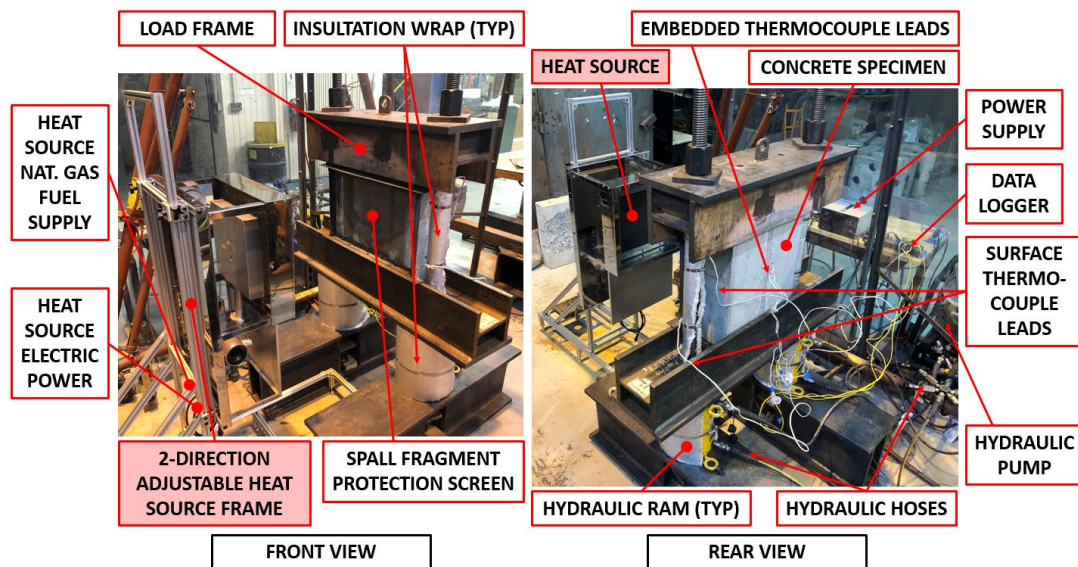


Figure 7: Self-reacting axial and heating load frame

Surface thermocouples were placed at the specimen width centerline, located at the top and bottom of the heat exposed specimen area. The heater was ignited at a distance of 686 mm (27 in) and rapidly moved to the testing distance of 152 mm (6 in) from the concrete specimen.

3.3 Thermal Loading

The heat source consisted of an adapted commercial cooker heating element mounted to an adjustable heater position, track mounted sled support frame. Figure 8 shows the commercial company's 3D rendered model of the heat source in (a), and the actual delivered heater in (b). The heating element is a natural gas fueled radiant panel heater which includes: a blower to optimize the fuel to air ratio, an electrical controller for fuel mixing and ignition, and an elevated rectangular fuel-feeder box topped with the radiant panel grill. Figure 8 (c) and (d) show the two different radiant panel grill materials used for testing, with (c) being a permeable metal foam material (used for the F1 heat flux curve) in a post heat cycling fatigue failure condition and (d) a compressed metal fiber material (the F2 and F3 heat flux curve grill material). Figure 8 (e) show the location of the feeder box pinch weld failure from the F2 heat flux curve set up, the radiant grill support frame to fuel mixing box seam experienced a heat cycling fatigue failure at testing pressure after 4 specimen tests. The pinch welded seam failure was rectified with an increase in the number of pinch welds, resulting in the F3 heat flux curve.

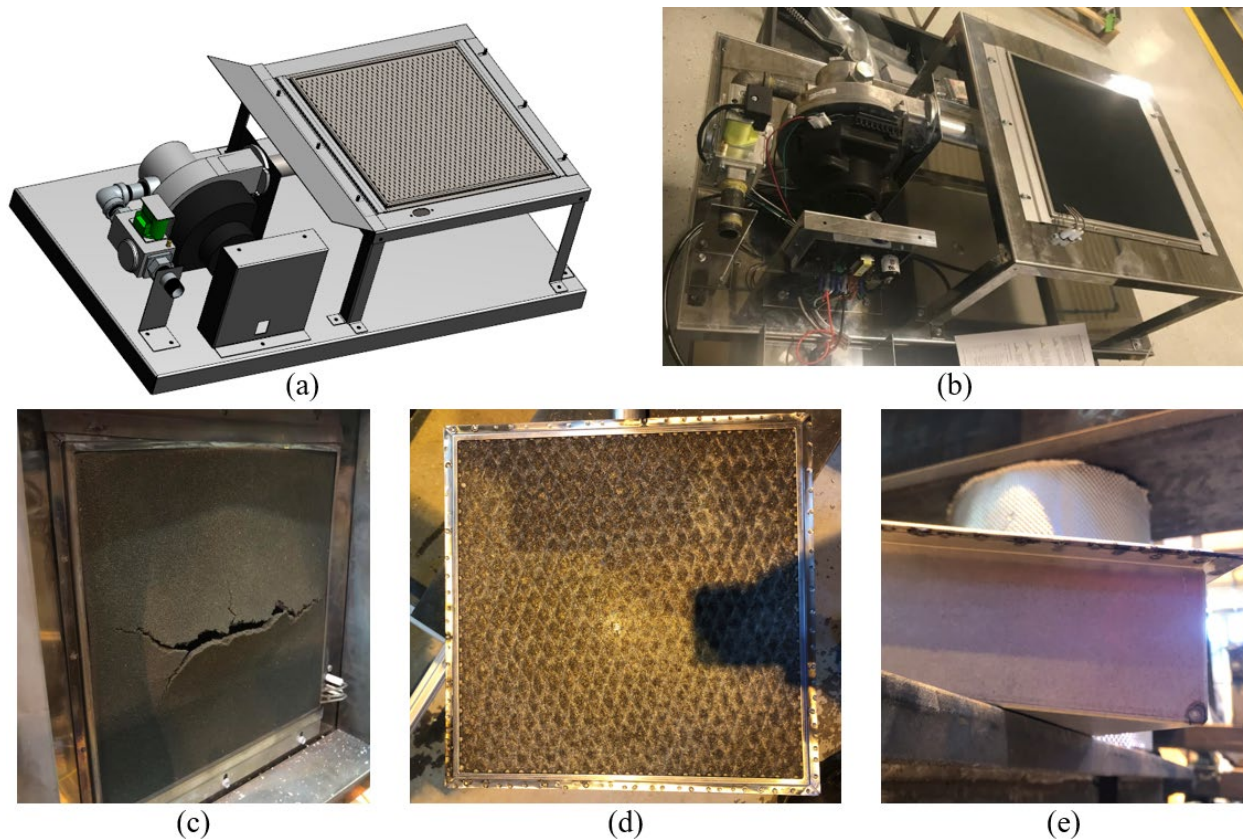


Figure 8: Heat source configurations (a) concept model (b) actual (c) F1 grill material failure (d) F2 and F3 grill material (e) F2 failure location

The heat source is mounted on a support frame to allow for three-dimensional adjustment. An extruded aluminum T-slot cross-section frame element was used to assemble the heat source support frame. A sled and track system to allow rapid movement of the heat source in the direction normal to the exposed specimen surface was integrated into the heat source support frame. Rapid standoff closing was needed to reduce the effect of heat source ignition on the sample before the

initiation of the calibrated heat flux curve, while also adding an element of safety during ignition with increases standoff between specimen and heater. The heater was ignited at a distance of 686 mm (27 in) and rapidly moved to the testing distance of 152 mm (6 in) from the concrete specimen.

Calibration was performed using the setup shown in Figure 9. The heat flux delivered to the sample surface was recorded using a water-cooled Hukseflux SBG01 heat flux meter, which was flush face mounted through a 19 mm thick x 457 mm wide x 610 mm high (0.75 in thick x 18 in wide x 24 in high) steel plate. The plate width and height were matched to the dimensions of the concrete specimen's heat exposed surface to maintain a similar area to control for convective effects around the heater, loading frame, and specimen, and to duplicate the radiation feedback loop between the heating source, protection screen, and test specimen. The radiometer mounted plate was located in the loading frame, and the same measurements and adjustments listed in the experimental procedure, including placement of the protective screen, were repeated for calibration.

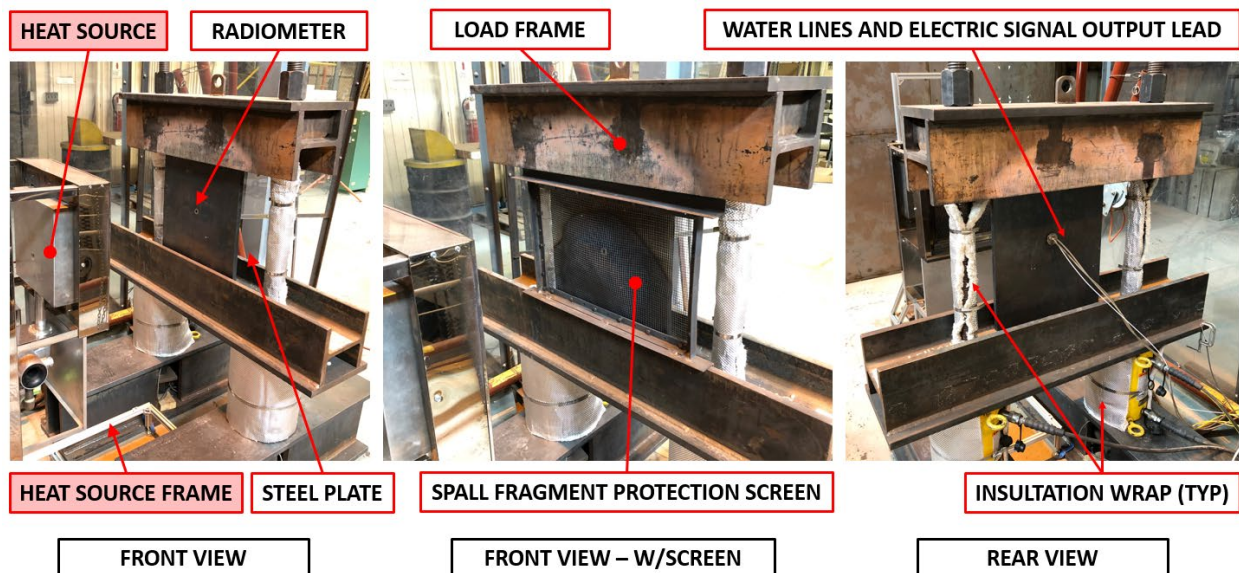


Figure 9: Testing apparatus heat flux calibration setup

Figure 10 shows the three unique heat flux time history curves for the three different heating source configurations used during testing. Three configurations of the heating source were used, due to initial variations in the radiator grill material and fuel feeder enclosure. The calibration curves are plotted with the ASTM E1529 hydrocarbon fire curve which is defined as a heat flux of 158 kW/m^2 ($\pm 8 \text{ kW/m}^2$) reached within the first 5 minutes and maintained throughout the test duration [38]. The ASTM E1529 standard is used as a representation of the rapid heat development and energy output of a standardized hydrocarbon pool fire; consistent with gasoline and diesel fuel spill fires that would be seen in fires resulting from roadway vehicle collision. The heating curves used in our experimentation do not meet the ASTM E1529 standard at the equipment-safe testing standoff, however the delivered thermal load was sufficient to exhibit explosive concrete spalling.

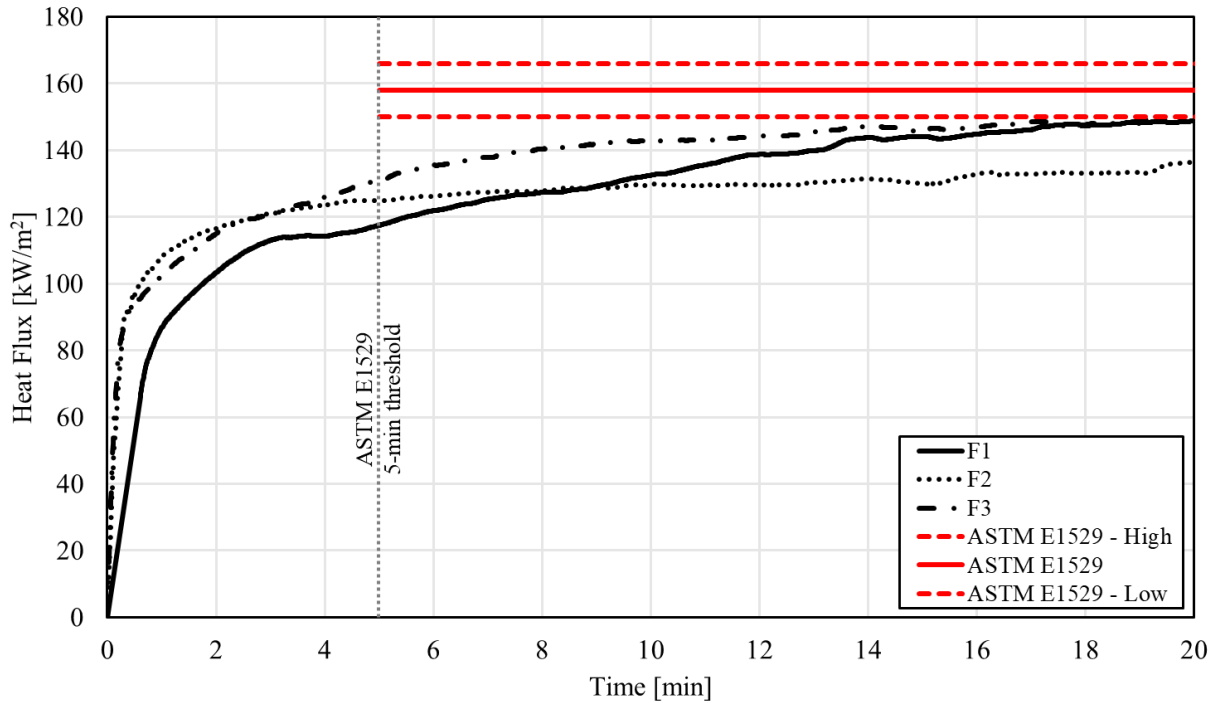


Figure 10: Calibrated heat flux time history curves including reference to ASTM E1529

3.4 Applied Axial Loading

The specimens were subjected to axial load to represent typical in-service stresses for load bearing concrete elements. The axial load level was varied from 14% to 19% of the nominal compressive strength of the concrete for the standard loaded specimens, and 1%, 3%, 27%, and 29% for the axial variation subset. The axial load was applied with two hydraulic jacks prior to thermal loading and maintained throughout the experiment. The load variance between the two jacks was less than 7% (with the maximum variation between the two jacks due to the low load axial variation cases at less than 3% f'_c while the mean variation between jacks was 4%), while the axial variation during the loading cycle was maintained below 4%. The variation in axial load is attributed to increase due to thermal expansion of the specimen heated face, limitation in precision of the hydraulic fluid pump, and some slop in the threaded rod connections. The axial load subset was included to isolate the axial stress contribution to surface spall. Four specimens were tested: two at minimal load, compared to the typical specimen load, and two at nearly double the typical specimen load. Comparison of the axial variation results are given in the results tables and specifically Table 4. And, the axial demand for all tests is summarized in Table 5.

Figure 11 shows the total axial load time histories for all specimens. Grey lines indicate spalled panel specimens, while black lines indicate no-spall panel specimens. The time histories were halted at the time of spall occurrence, if applicable. All panel specimen axial load histories exhibit a positive slope at the start of heat exposure, showing an immediate thermal expansion effect on the pressure controlled hydraulic pump load delivery assembly and resultant load cell record. Only one of the doubled axial load specimens was available (C1-4.1-08.6-F2), the second high axial

load case had corrupted data. As can be seen in the two low axial load variation cases explosive spalling did not occur, but the variation in the load during testing was much greater than the standard load cases. This low axial load deviation from the initially set value was a functional limitation of the hydraulic pump used to load the specimens. Typical load variation due to thermal effects was at approximately 4%, when excluding the low axial load tests.

In Figure 11, C1-4.1-09.0-F1 was the panel specimen that exhibited small area delamination sluffing spall within two minutes of heat exposure. The C1-4.1-09.0-F1 spalling behavior was not explosive in nature, and the typical crackling behavior that indicated impending explosive spalling was not observed. C1-4.1-09.0-F1 heating was extended to 15 minutes, beyond the typical spall occurrence within 10 minutes of heat duration, before termination of the test. Within the standard load specimens, under the load time histories in Figure 11, we see that the non-spalled cases are bounded by spalled cases with slightly higher and slightly lower axial loads, indicating that loading stress alone was not a predictor. In the axial load variation case we see that the low axial load cases did not exhibit explosive spalling behavior while the double loaded cases did. We can conclude that mechanical loading stresses do play a part in explosive thermal concrete spall.

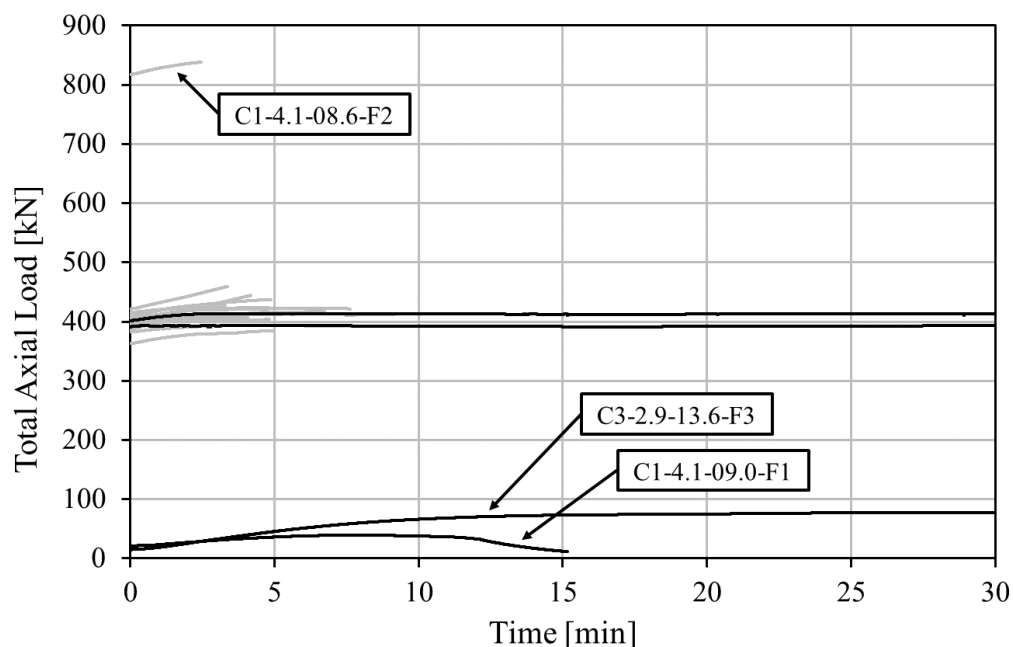


Figure 11: Total axial load time histories for all specimens

All C2 specimens were tested at the 14-18% of compressive strength axial load level and explosively spalled regardless of moisture characteristics (even at MC as low as 2.4%). The C2 specimens demonstrated consistent spalling behavior regardless of the heating curve that was used to conduct the test; therefore, the slight variations in the heating curves in Figure 10 did not discernably influence the observed spalling behavior. Three specimens (C1-3.3-16.7-F1, C1-3.0-13.7-F2, and C3-2.9-13.6-F3) survived 45 minutes of heat exposure without any spalling. A fourth specimen (C1-4.1-09.0-F1) exhibited some minor delamination spalling in two locations on the heated face; however, these small concrete chips fell off rather than exploded off the heated face

during the test. This panel was therefore marked in Table 5 as not having explosively spalled due to the observed mechanism during testing. Neither the curing method nor the reinforcing detail showed any discernable difference in the spalling behavior within this limited sample set. Variation in axial load, however, did produce a noticeable difference in explosive spalling behavior even within similar moisture characteristics.

CHAPTER 4 – RESULTS AND DISCUSSION

Of the twenty-four specimens that were tested, twenty exhibiting thermally-induced explosive spalling behavior, one exhibited minimal non-explosive spalling, and three showed no spalling behavior during testing (with residual surface cracking observed after being subjected to at least 45 minutes of heat exposure). The experimental results in Table 5 report the following (with specimens labeled and ordered identically to the pre-testing condition summary in Table 4):

- Confirmation of explosive spalling occurrence
- Axial demand on each specimen as a percentage of the nominal compressive strength
- Time of explosive spalling (to the nearest 30 seconds) from the start of active heating
- Heat flux at the time of spall per the calibration curves in Figure 10
- Total imparted energy at the time of spall (calculated as the area under the heat flux curves in Figure 10 up to the time of spall)
- Temperatures recorded at the 25.4-mm (1-in) depth from the heated surface embedded thermocouple
- Depth of spalling measured at the center of the specimen (corresponding to the location of the calibrated heat flux measurements plotted in Figure 10) following the completion of the test and full cooling
- A figure list for each specimen temperature time history plotting

A post-test, perspective-corrected photo of the heated face of each specimen is provided in Table 6. A black felt-tipped marker was used to highlight the visible cracking on the heated face for these photos. Color coding in Table 6 is used to denote differences among specimen properties (curing method and reinforcement detail), as well as, the level of applied axial load.

The twenty specimens that exhibited explosive heat-induced spalling all spalled within 9 minutes of exposure to active heating per the radiant heat flux curves in Figure 10. There was no sudden loss of axial resistance in any spalled panel specimen, as axial loading was maintained for several minutes beyond the onset of spalling. For specimens that explosively spalled, heating was stopped within a few minutes after spalling occurred by turning off the burner and safely retracting it along its sled track. For standard loaded specimens that did not exhibit explosive spalling, heating was continued for at least 45 minutes to ensure sufficient thermal penetration without the observation of spalling.













Table 5: Summary of heated panel test results

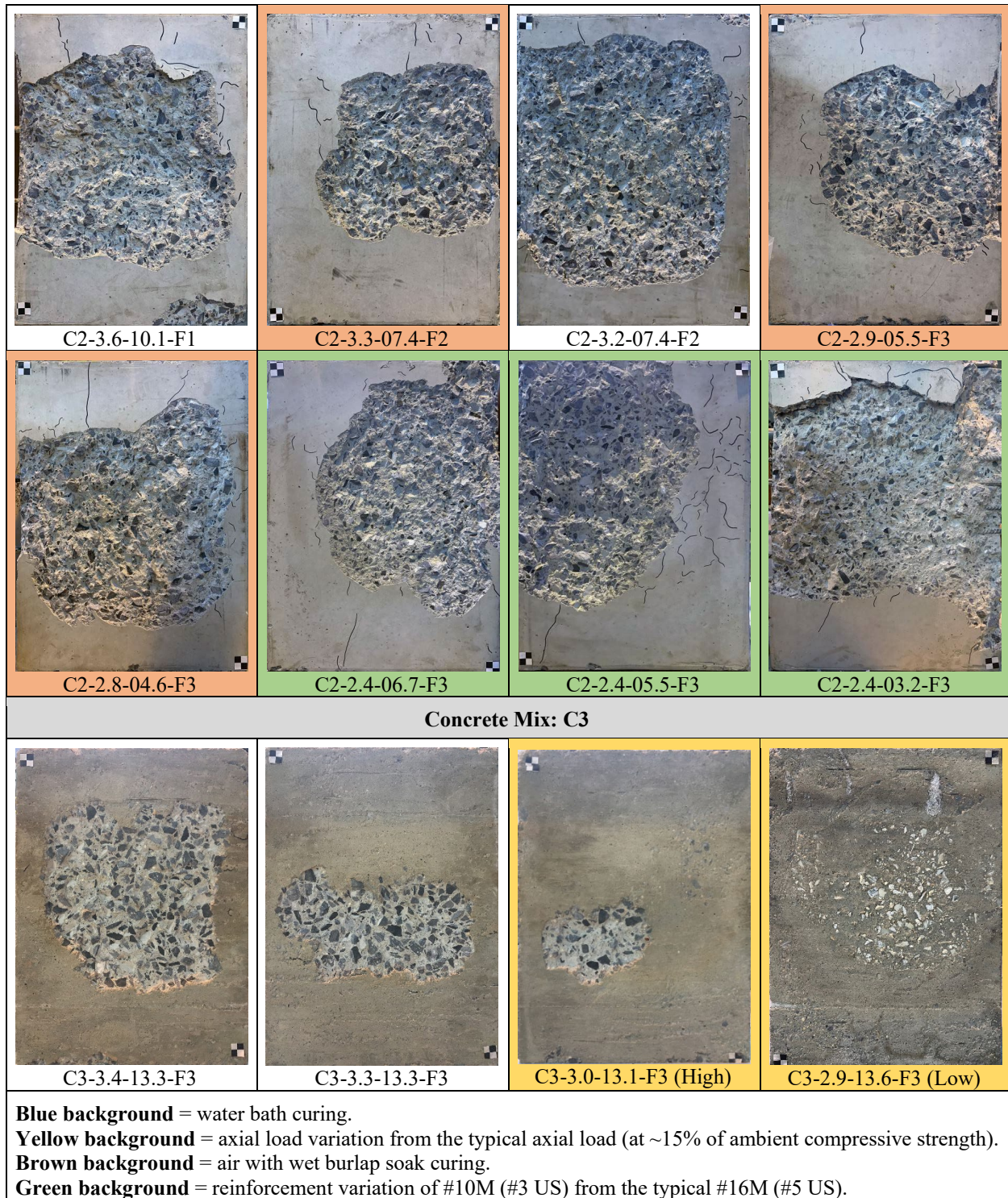
Label	Spall	Axial Load per nom. f'_c	Spall Time	At Approximate Spall Time			Spall Depth at Center
				Flux	Total Impart. Energy	Temp. 25.4mm Depth	
		[%]	[min]	[kW/m ²]	[kJ/m ²]	[°C]	[mm]
C1-4.1-15.6-F1	Y	14	4.5	115	7.1	70.5	15
C1-4.1-09.0-F1	Y	1	NO EXPLOSIVE SPALLING				
C1-4.1-08.6-F2	Y	29	2.4	119	3.9	35.6	15
C1-3.8-13.2-F1	Y	14	8.6	128	15.5	139.8	22
C1-3.8-12.4-F1	Y	14	6.1	122	10.3	128.3	22
C1-3.3-16.7-F1	N	14	NO EXPLOSIVE SPALLING				
C1-3.3-03.4-F3	Y	14	2.1	116	3.2	30.0	13
C1-3.0-13.7-F1	N	14	NO EXPLOSIVE SPALLING				
C2-4.6-18.5-F1	Y	18	5.1	118	8.3	85.3	14
C2-4.2-14.9-F1	Y	17	4.0	114	6.2	X	16
C2-3.9-15.4-F1	Y	18	6.6	124	11.3	88.0	23
C2-3.9-10.8-F1	Y	17	5.4	120	8.9	X	22
C2-3.6-10.1-F1	Y	17	5.5	120	9.1	X	23
C2-3.3-07.4-F2	Y	18	3.1	121	5.3	61.0	19
C2-3.2-07.4-F2	Y	17	4.9	125	9.0	95.7	21
C2-2.9-05.5-F3	Y	17	3.6	124	6.2	73.7	17
C2-2.8-04.6-F3	Y	17	4.3	127	7.6	74.8	19
C2-2.4-06.7-F3	Y	16	4.5	128	8.0	70.2	16
C2-2.4-05.5-F3	Y	17	7.0	138	13.6	127.3	24
C2-2.4-03.2-F3	Y	16	7.8	140	15.5	130.8	26
C3-3.4-13.3-F3	Y	15	3.8	125	8.0	100.7	10
C3-3.3-13.3-F3	Y	16	3.4	122	5.9	71.0	11
C3-3.0-13.1-F3	Y	27	5.0	125	9.2	X	13
C3-2.9-13.6-F3	N	3	NO EXPLOSIVE SPALLING				

Label: CX (Conc. Mix) - X.X (Moisture Content %) - XX.X (Act. Vapor Density g/cu. m) - FX (HF Curve)

X: Indicates sensor malfunction

Table 6: Post-test perspective-corrected photos of the tested face of each specimen.

Concrete Mix: C1			
			
C1-4.1-15.6-F1	C1-4.1-09.0-F1 (Low)	C1-4.1-08.6-F2 (High)	C1-3.8-13.2-F1
			
C1-3.8-12.4-F1	C1-3.3-16.7-F1	C1-3.3-03.4-F3	C1-3.0-13.7-F1
Concrete Mix: C2			
			
C2-4.6-18.5-F1	C2-4.2-14.9-F1	C2-3.9-15.4-F1	C2-3.9-10.8-F1



Explosive spalling generally presented audibly as a loud “bang” with a large amount of chip and chunk debris suddenly being blasted into the protection screen. The onset of spalling in the C2 specimens was noticeably louder and more violent than for C1 or C3, and the C2 specimens gave little visible or audible warning before exploding. As shown in the photos in Table 6, the more

explosive C2 spalling reaction generally resulted in a greater amount of the spalled concrete on heated face. C1 samples typically had some small “pops” of dust and sand sized particulate debris accompanied by “fizzling” noise in advance of explosive spalling, in effect warning of an imminent explosive spall event. Spalling in the C3 specimens was sudden like the C2 specimens, but less violent, as demonstrated by the smaller area of lost concrete on the spalled C3 panel faces in Table 6.

Figure 12 plots the dataset by RH (a) and VD (b) against the MC for all specimens in Table 5. Figure 12 uses diamonds for C1, circles for C2, and triangles for C3. In Figure 12 (a) the axial variation panel specimens are included with an open shape, lacking infill for the marker shape. Figure 12 (b) omits the axial variation cases, but includes a cubic regression for spalled specimens of standard load across all concrete mixes and a $\pm 99\%$ confidence interval for the standard error of the regression. When plotting MC to RH two specimens, from the C1 axial load variation set, plot on top of each other, as indicated by the labeled arrow, however these specimens express a difference of 1.6 g/m^3 in VD. Additionally, we see that spalling and non-spall behavior appears to overlap in the MC to RH in Figure 12 (a), while a demarcation between spall and non-spall cases is suggested in the MC to VD in Figure 12 (b).

Concerning the non-spalled panel specimens, a similar initial moisture state to the non-spalled C1 specimens was tested using two specimens from C3 with: 68% RH, 13.3 g/m^3 VD, and 3.4% MC; and 68% RH, 13.3 g/m^3 VD, and 3.3% MC, respectively, however these specimens spalled. When comparing the RH and MC of the C1 to C3 specimens at these high RH conditions, it appears that the spalled C3 specimens were at a higher moisture state than the non-spalled C1 specimens, however comparing the VD to MC moisture states we see that the C1 specimens were in fact the higher moisture state; giving more credibility to using VD instead of RH. There appears to be an argument for further testing to assess whether a spalling threshold may be better defined by VD as a function of MC instead of MC alone. Because of the limited non-spall results, herein, there would be little confidence in a defined initial moisture condition state to predict the occurrence of spalling behavior under the thermal and axial loading used in this study.

These differences between the overlapping specimens in RH but not in VD plotting, the larger spread between points, and the suggested demarcation between spall and non-spall occurrence in the VD plotting represent the authors’ arguments for reporting VD instead of RH. The RH, through saturated vapor density normalization, removes the direct quantity of water vapor and the material temperature from reporting, while VD does not. RH may prove to be important in comparison between spalling and non-spalling concrete cases, however the ambient temperature of the material shortly before heat testing should be included for detailed initial moisture state description.

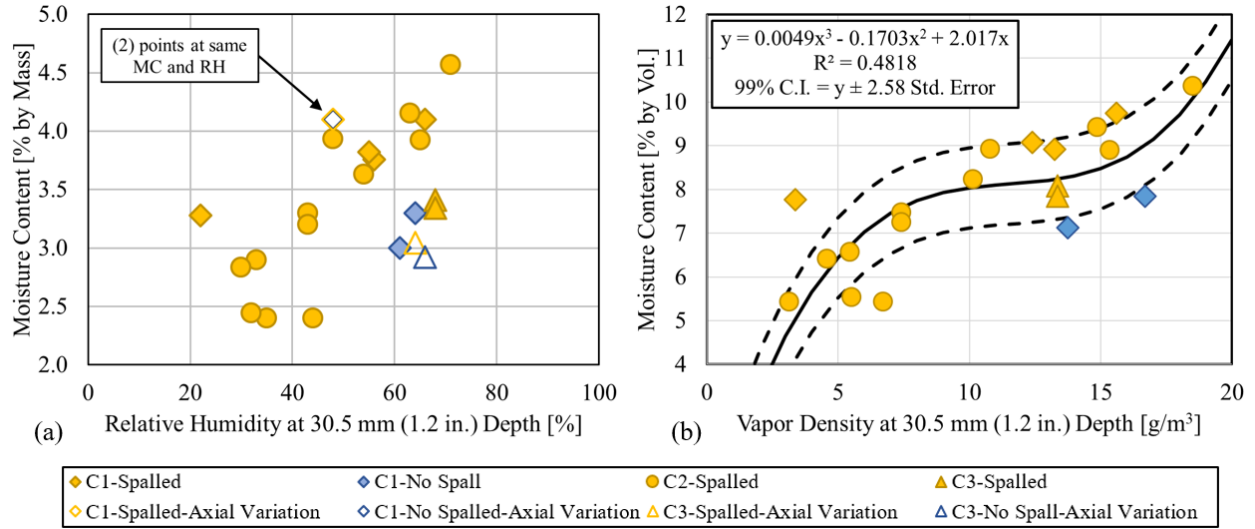


Figure 12: RH and VD compared to MC results summary

Concerning Figure 12 (a), Hertz defines the MC threshold being between 3.0% and 4.0% depending on the concrete mix design, while Eurocode 2 and 4 define two different thresholds, the most conservative at 2.5% [18,39,40]. These thresholds appear to hold true for C1, however C2 spalling was observed at MC percentages below both definition limits, consistently. The RH/VD of the spalled C2 specimens were significantly lower than the non-spalled C1 specimens, which may indicate that the occurrence of spall may be dependent on the form in which water is present in the concrete (e.g. liquid or vapor). Looking more closely at the non-spalled cases in Figure 12, two C1 specimens did not spall with initial moisture states of: 64% RH, 16.7 g/m³ VD, and 3.3% MC by mass; and 61% RH, 13.7 g/m³ VD, and 3.0% MC by mass, respectively. The MC of these non-spalled specimens fall within the Hertz defined MC by mass threshold zone of no-spalling behavior, which was our initial interpretation of the behavior. However, Mindeguia et al. (2011) have shown high moisture condition concrete specimens to exhibit reduced pore pressures under heating when compared with lower moisture state concrete specimens of the same mix design; justifying the findings as being resultant of early cracking due to water expansion during early stage heating [41]. These cracks would create ventilation routes for vapor, impeding large pore pressure buildup, in effect increasing the concrete gas permeability. Overall, the results shown in Figure 12 are suggestive that MC alone is insufficient for the prediction of thermally induced explosive concrete spalling behavior under a representative hydrocarbon fuel fire scenario.

Concerning Figure 12 (b) for the standard axial load dataset by MC and VD, the MC was converted from percent by mass to percent by volume via the dry bulk density determined under the ASTM C642 standard reported in Table 3. The conversion was to allow for more closely aligned comparison between the liquid and vapor phases of water at initial condition in the concrete panel specimens. Typical figures in the literature which compare water phase distribution in concrete use MC and RH, and show cubic trend behavior [42]. Therefore, the dataset presented in Figure 12 (b) uses a cubic regression for the spalled specimens with a zero intercept definition. In addition to the cubic regression, the standard error of the spalled dataset was included and the 99% confidence interval boundaries were plotted above and below the cubic regression. The non-spalled specimens, under the standard axial load, interestingly, plot outside of the -99% confidence

interval. Because Mindeguia et al. (2011) also observed similar non-spalling behavior in high RH/VD specimens at MC that would otherwise be expected to spall, there may exist a spalling threshold defined by the initial moisture condition. The data present herein attempts to suggest a first attempt at that threshold definition, defined similarly to the regression and confidence interval in Figure 12 (b), for greater than 10 g/m³ VD concrete condition.

The time temperature histories for all specimens at the 25.4-mm (1-in) depth thermocouple are plotted in Figure 13, where spalled cases are denoted with grey lines and non-spall cases with black lines. The Figure 13 (a-b) plots are identical, only differing in time scale for perspective. The Figure 13 (c-e) plots group the results of the Figure 13 (b) plot by concrete type and adjust the raw temperature to a change in temperature over the ambient material temperature. As indicated in Table 5, the 25.4-mm thermocouple failed to produce clean data for four of the panel tests marked with a corresponding “X” – those cases were therefore excluded from Figure 13. Time histories for spalled cases are terminated at the time spalling initiated, which was signified by a sudden jolt in the raw temperature time history data. Despite the modest difference in thermal properties between C1 and C2/3 (see Table 3), the plots in Figure 13 show no discernable variation in the rate of temperature increase at the 25.4-mm (1-in) depth as a function of concrete type. Differences in actual temperature at the same time of exposure can be observably attributed to differences in the initial material temperature (which varied due to the time of year and daily atmospheric conditions at which these specimens were tested).

The Figure 13 (c) plot show similar curves for the two C1 specimens that did not spall under the standard applied load (C1-3.3-16.7-F1 and C1-3.0-13.7-F1), which had MC near the 3% spall limit suggested by Hertz [39] and relatively high actual VD compared to their spalled C1 counterparts. The other cases that did not spall (C1-4.1-09.0-F1 and C3-2.9-13.6-F3) again were presumed to not exhibit explosive spall due to very low applied axial load, and any correlations of temperature increase with MC and VD are therefore inconclusive. It is interesting to note, however, that the distinct S-bend in the C1-4.1-09.0-F1 temperature time history initiated at a reasonable expectation of time delay for temperature reaching from the depth of minimal delamination spall of 6 mm to the 25.4 mm embedded thermocouple sensor.

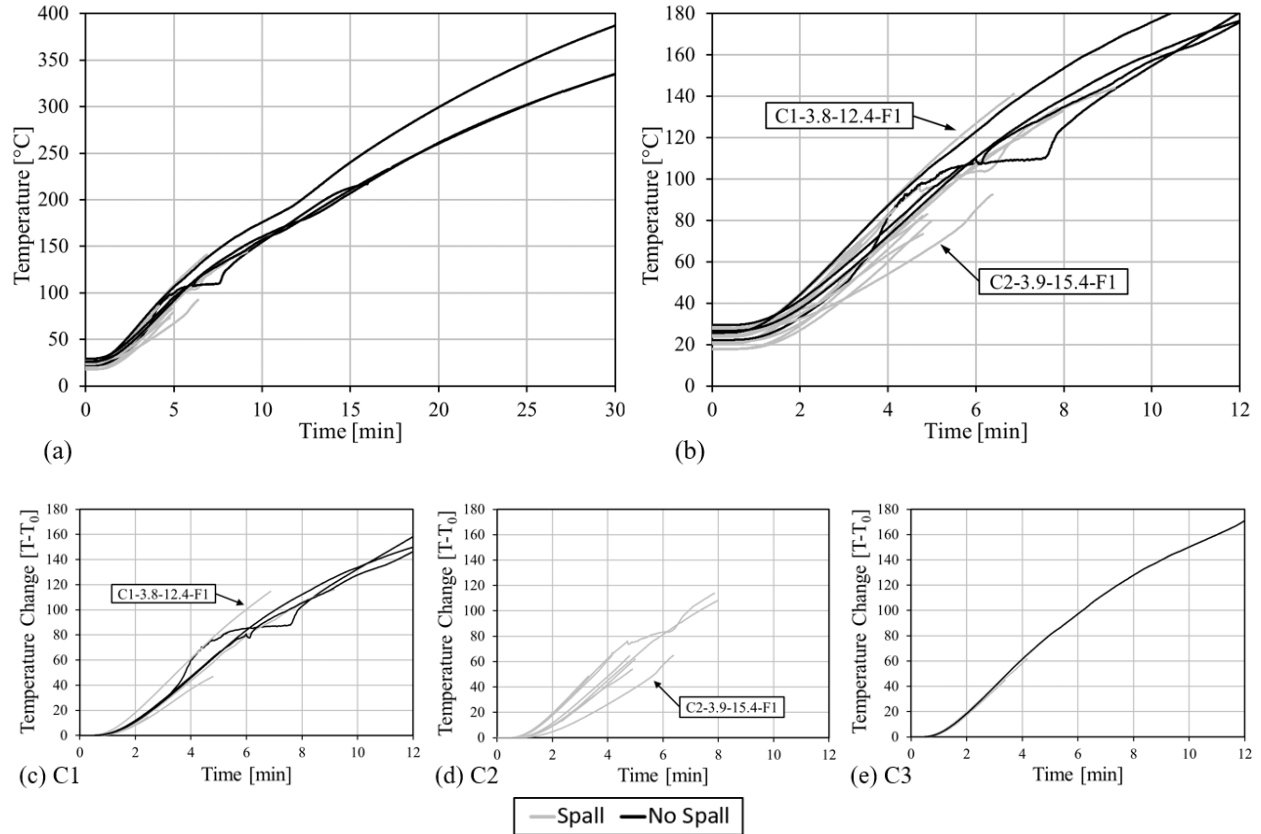


Figure 13: Temperature time histories at 25.4-mm depth embedded thermocouple for (a) all specimens up to 30 minutes of exposure, (b) all specimens up to 12 minutes of exposure, and (c-e) grouped by concrete mix

4.1 Effects of Heating Time History

The plots from Figure 13 are reproduced in Figure 14, but are instead color coded by the applied heating curve defined in Figure 10. Figure 14 (a-b) show all specimens together within differences in the time scale, while plots Figure 14 (c-e) differ from (a-b) by adjusting the raw temperature to a change in temperature over ambient and group according the applied heating curve. Temperature increases at 25.4-mm from exposure to heating curves F2 and F3 showed greater consistency than those for heating curve F1. The larger spread in the temperature histories under the F1 curve can be explained by fluctuations in the grill material that was originally used for the burner face. The metal foam material used in the F1 burner face was prone to greater heat-induced deformation (and eventually failed as a result) during heating than the metal mesh material used to obtain F2 and F3. These deformations could slightly change the standoff from the heat source to the concrete specimen during testing – for example, cases C1-3.8-12.4-F1 and C2-3.9-15.4-F1 appeared to experience slightly greater and slightly lower heat flux, respectively, due to the deformations of the F1 burner face material. Otherwise, Figure 14 shows that all other specimens with 25.4-mm temperature data showed relatively consistent rates of temperature increase when grouped according to heating curve. More importantly, neither Figure 13 nor Figure 14 show observable

differences in temperature increase at a 25.4-mm depth between cases that explosively spalled and those that did not.

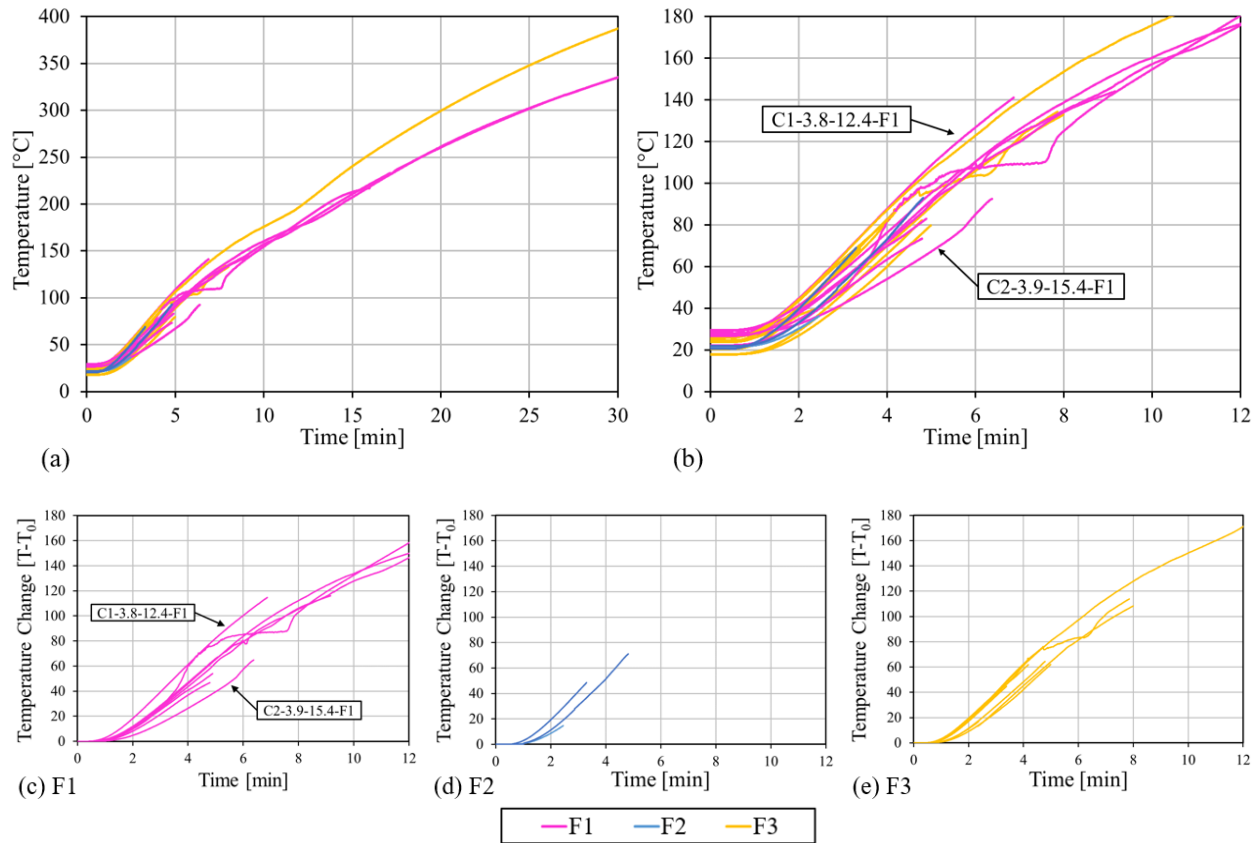


Figure 14: Temperature time histories at 25.4-mm depth for (a) all specimens up to 30 minutes of exposure, (b) all specimens up to 12 minutes of exposure, and (c-e) grouped by heating curve

Figure 15 plots the raw temperature time histories from top surface thermocouple sensor for all tests. Figure 15 (a-b) show the same plot of all panel specimen top surface temperature records together with a difference in time scale between them, while Figure 15 (c-d) group the time histories by heating curve. Figure 15 (c-d) shows the F1 shallower than the F2 and F3 curves, as expected. In the Figure 15 (c-d) plots, we see that the F1 and F2 temperatures are relatively tight between tests, while the F3 temperature histories show more variation. The dispersion in the top surface thermocouples in F3 is likely due to movement of the surface thermocouples during heat exposure. During some tests the thermal expansion of the protection screen, initial particulate debris fizzling behavior, and in some tests, physical movement to relocation the sensor have cause alterations in the temperature records. The variations and differences here still show relatively similar performance between the heating curves from a different, though a less rigorous standard when compared to the embedded histories shown in Figure 13 and Figure 14, perspective. The temperature profiles are consistent with the temperature expectation resulting from the heat flux curves presented in Figure 10. The reference ASTM E1529 standard requires a minimum of 815°C

at 3 minutes and between 1010°C and 1180°C at and after 5 minutes [38]. Figure 10 notes the testing performance of this experimental program as less than ASTM E1529 standard under heat flux, and this is reinforced when examining the surface temperatures in Figure 15.

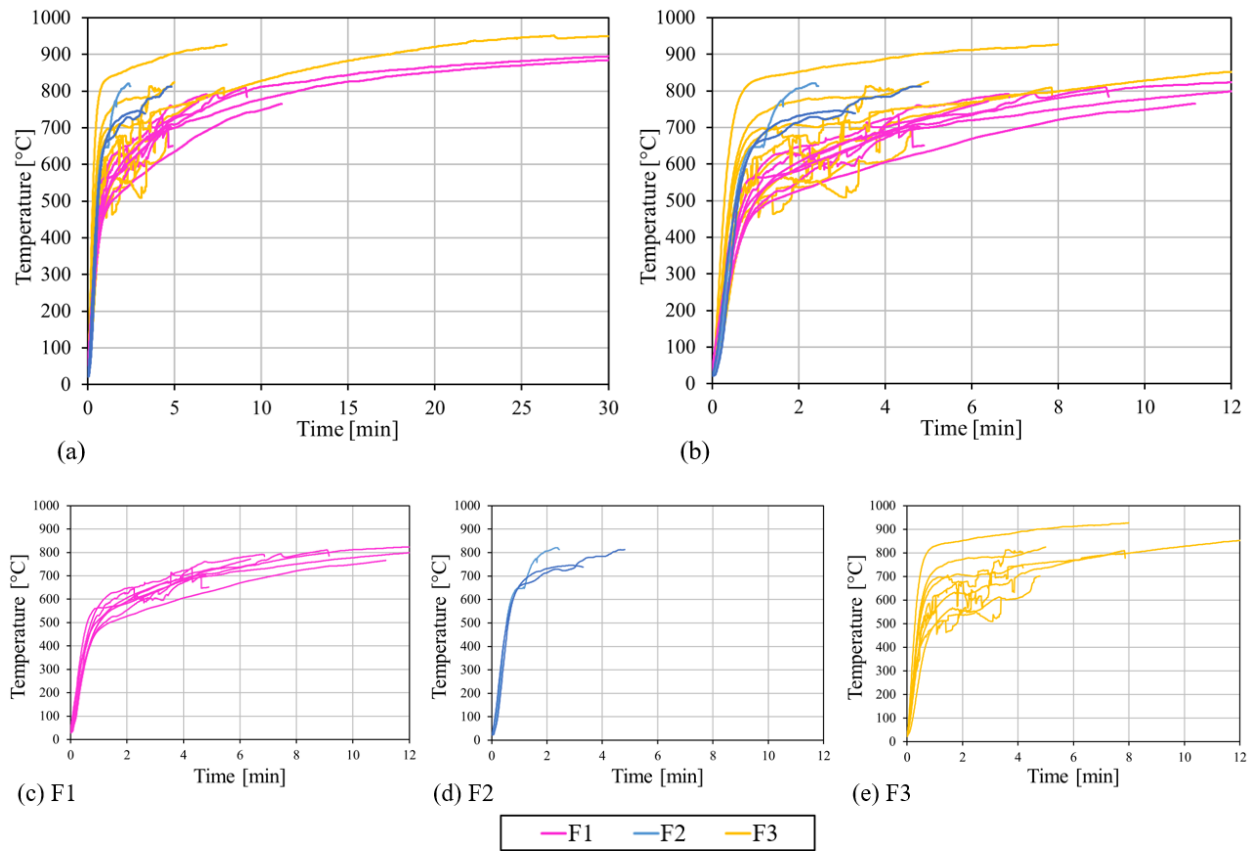


Figure 15: Surface temperature time histories at top of exposed face location (a) all specimens up to 30 minutes of exposure, (b) all specimens up to 12 minutes of exposure, and (c-e) grouped by heating curve

Figure 16 plots the imparted energy to the panel specimens from the burner against (a) the spall time, (b) the spall depth at the center of the specimen, and (c) moisture content percentage by mass. Figure 16 (d) plots the spall depth against the moisture content percentage by mass. Similarly to Figure 12, the points are grouped by concrete mix (denoted by the marker shape) and the applied heat flux curve (denoted by color) for comparison. The points plotted in Figure 16 represent only the spalled cases excluding the axial variation cases to maintain comparison baseline. The imparted energy is defined by the area under the individual heat flux curve, defined in Figure 10, applied to the specimen from initiation up until the time of spall occurrence.

The imparted heat energy to spall time plot, Figure 16 (a), shows linear behavior for all spalled specimen results, with an R-squared of 0.9578 for a standard linear regression with a zero intercept, indicating very similar performance between the different heating source configurations (i.e., heat flux curves). The similar performance between the heating curves, defined in Figure 10, allows like-for-like comparison between specimens tested under the differing F1 through F3 heating curves. Figure 16 (b) includes a second degree polynomial regression with an R-squared of

0.5610 indicating relatively poor agreement between spalling depth to imparted energy. The lesser degree of good-fit for the spall depth to imparted energy is indicative a greater sensitivity of spall depth to the moisture condition and concrete mix. Figure 16 (c-d) shows the moisture content percentage by mass against (c) the imparted energy and (d) the spall depth. A distinct segregation by heating curves becomes apparent in the imparted energy and spall depth when plotted against the moisture content. The longer the duration of heat exposure to achieve spalling is proportionally related to the spalling depth, with longer durations resulting in deeper spall depths. This could be explained by lower concrete moisture states, requiring more depth to accumulate enough water to fully saturate the voids and form a moisture clog. In turn, the greater the temperature penetration required to gain the required moisture to form a clog, the deeper the resulting location for: clog, peak pore pressure, and resulting spall depth.

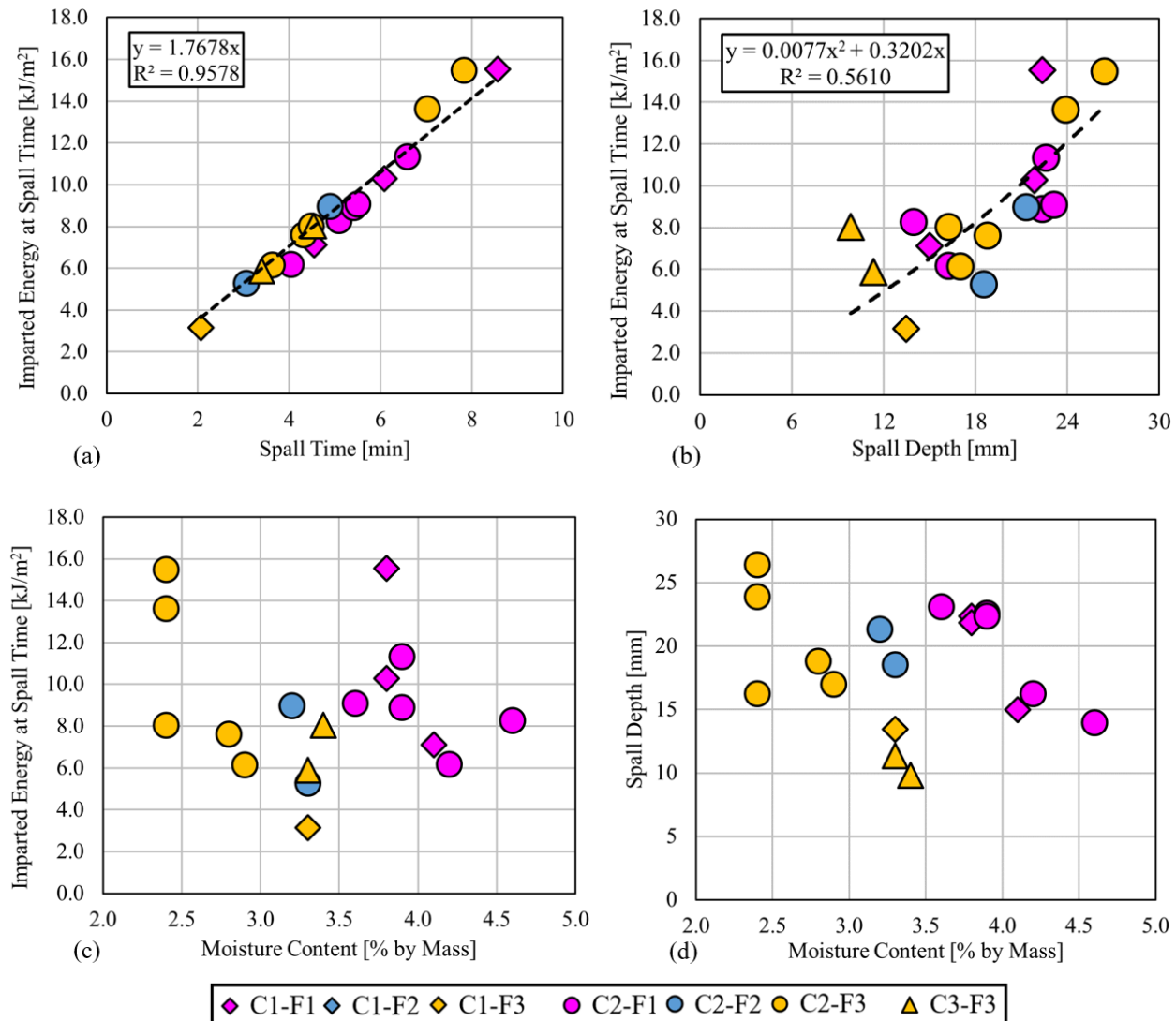


Figure 16: Spalled specimens at standard axial load: imparted energy against (a) spall time (b) spall depth at the center of the panel specimen heat exposed area (c) moisture content; and (d) spall depth against moisture content.

Ultimately, the performance of the testing apparatus illustrated in Figure 11 and Figure 13 through Figure 16 show some variation between the heating curves and test-to-test setup, however there is a strong correlation between imparted energy and spall time and between temperature records. As such, the comparison between concrete panel specimens across mix design, heating curve application, and moisture condition presented in this study was determined to be reasonable in exploring thermally-induced explosive concrete spalling behavior. Temperature time-history, in effect thermal stress, alone did not present an indicator of spall occurrence.

4.2 Effects of Varying Moisture Conditions at Similar Axial Load

Following the path from the temperature time history plots (presented in Figure 13 and Figure 14) and the suggested influence of the moisture state (presented in Figure 12 and Figure 16), the temperature time histories from the 25.4-mm (1-in) depth embedded thermocouple are reproduced once again in Figure 17, but are color-mapped by MC in (a and c-e) and by VD in (b and f-g). Figure 17 (c-g) similarly to the previous embedded temperature plots, adjusts the raw temperature to a change in temperature above ambient. Reviewing Figure 17 (a and b) including all concrete mixes, we see that MC and VD show both high and low moisture conditions present spall and non-spall behavior, and also that high MC or VD show temperature histories that rise both faster and slower than low MC and VD conditions. C2 panel specimens, shown in Figure 17 (d and g), appear to present a trend of high MC and VD presenting slower temperature rise, suggestive that for some concrete mix designs the thermal penetration at high moisture states is slower than at lower moisture states. Figure 17 (e and h) present the two C3 specimens at relatively middling MC and VD, because only two standard load specimens were included for comparison to the non-spalled C1 cases at high RH/VD condition (see the discussion of Figure 12 for more detail). As we can see throughout the different divisions presented in Figure 17, we are again presented with no discernable trends in the temperature history as a function of either moisture state characteristic, nor identify and indicator for the occurrence of explosive spalling behavior.

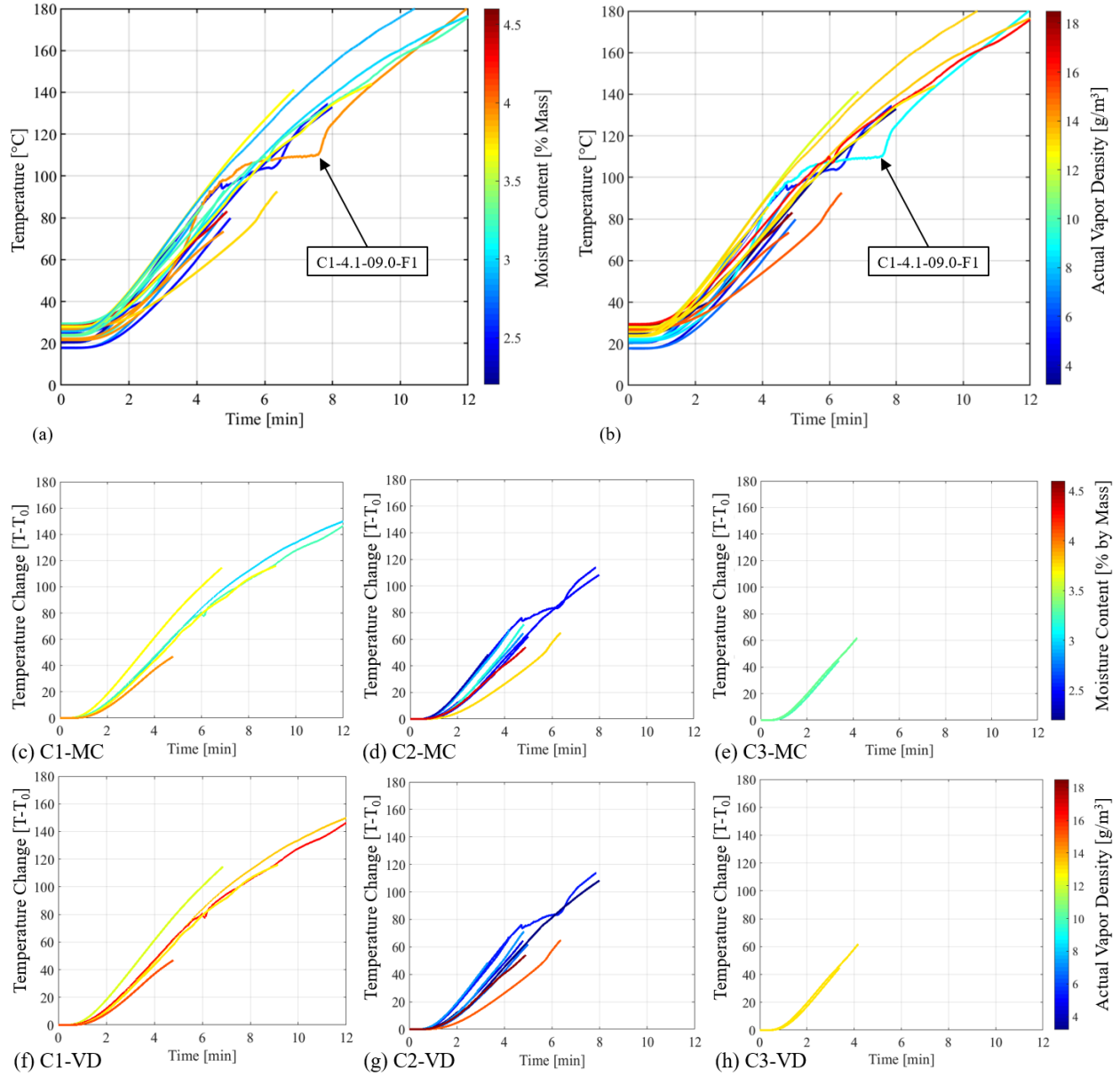


Figure 17: Temperature time history at 25.4-mm depth for all specimens, color-mapped by (a) moisture content and (b) actual vapor density by raw temperature; (c-e) moisture content and (f-h) vapor density by change in temperature above ambient

4.3 Effects of Varying Axial Load at Similar Moisture Conditions

Figure 18 (a) plots the axial load variation subset including: three C1 specimens with standard load, double load, and minimal/negligible restraining load; and three C3 specimens of standard load and the minimal/negligible load. The doubly loaded C3 specimen experienced a thermocouple failure and the temperature time history at the 25.4 mm (1 in) depth was corrupted; therefore not included. Figure 18 (b) plots the C3 panel specimens at reduced scale, as the C3 panel specimens included additional thermocouples within the spalled depth when compared with the C1 and C2

sets, for thermocouple depths of 0 mm (0 in), 12.7 mm (0.25 in), 6.4 mm (0.5 in), and 25.4 mm (1 in).

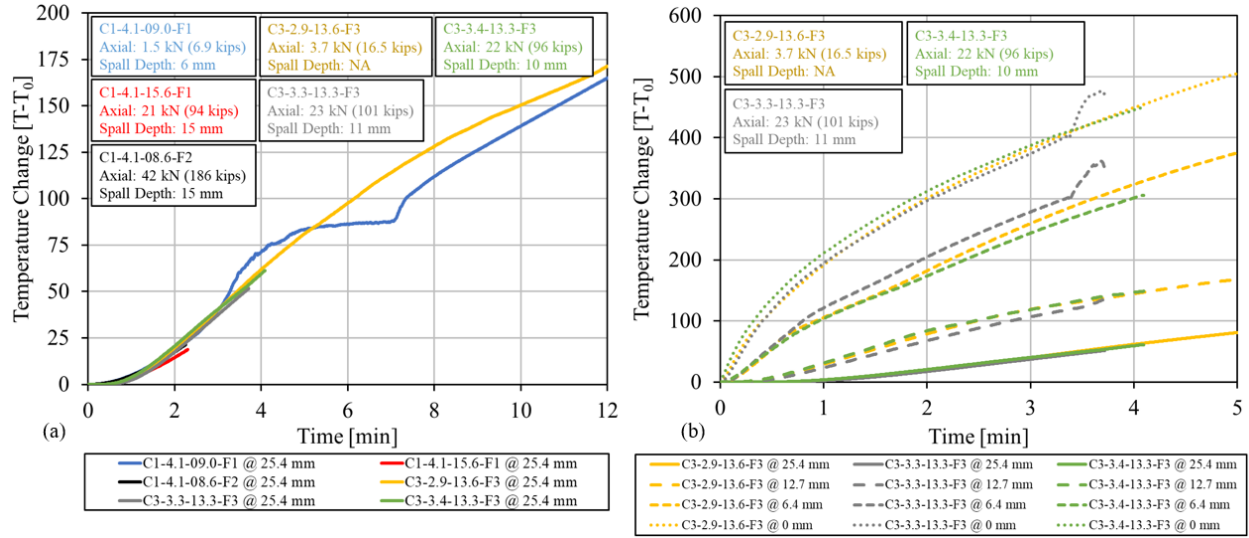


Figure 18: (a) Axial load variation subset 25.4-mm (1-in) embedded thermocouple sensor temperature comparison, (b) C3 all thermocouple sensor temperature time history comparison

Again, we see minimal differences between the temperature histories between specimens regardless of the mix design, illustrating the temperature and initial moisture conditions are insufficient for spall prediction. Specimens were selected for the axial variation subset such that their moisture conditions pre-heat exposure were similar, allowing for close comparison. Reducing the applied loading to a very small value (1-3% of nominal compressive strength) mitigated explosive spalling for C1-4.1-09.0-F1 and eliminated spalling altogether for C3-2.9-13.6-F3. The doubly loaded (27-29% of compressive strength) counterparts, C1-4.1-08.6-F2 and C3-3.0-13.1-F3, exhibited similar explosive spalling as other C1 and C3 panels that had comparable moisture characteristics but were tested at the lower 14-18% standard load level. These results clearly indicate that the level of applied loading and localized restraining stress of the heated face that, when combined with a rapid increase in pore pressure, contributes to a buildup of bursting stress toward explosive spalling. These findings are echoed in Kodur and Banerji (2021), where the influence of mechanical stresses in spall behavior are emphasized and validated using beam elements under flexural load as opposed to this study's axial loads [43].

Specimen C1-4.1-09.0-F1 follows the same temperature behavior at the 25.4 mm (1 in) embedded thermocouple as all of the other axial subset specimens until approximately 3 minutes. C1-4.1-09.0-F1 deviates from the typical temperature behavior of the other specimens after 3 minutes with a sharp temperature increases which is then followed by a plateau from 5 to 7 minutes. The rapid temperature rise was preceded by the minimal delamination spalling, occurring at approximately 2 minutes. Steep temperature increases are expected, via the ideal gas law, near moisture clog occurrence as the pore pressures increase. It is plausible that this sharp rise in temperature may be due to the movement of the moisture clog from the delamination spalling depth of 6 mm to the observation at the 25.4 mm thermocouple sensor with the plateau behavior indicating pressure

release due to increased permeability; explaining the lack of explosive spalling behavior for this specimen.

Figure 18 (b) plots all of the available C3 specimen thermocouple data from heat initiation to spall, and includes the no spall minimal axial loaded case (the continuous curves). The C3 specimens had thermocouples placed at depths closer to the heat face: 0 mm (0 in), 6.4 mm (0.25 in), 12.7 mm (0.5 in), and the standard across all specimens 25.4 mm (1 in) depths. C3 specimens present more detailed temperature information because thermocouples are placed within the spalling depth. Deviation between the different specimen temperature records at the closer to heat face, most notably the 6.4 mm (0.25 in) depth sensor, is exhibited, however the no spall case is bounded above and below by spalled cases. It is of interest that some of the thermocouple temperature records spike sharply near the occurrence of spall, however this behavior was not consistent across specimens and could be a function of the tolerance of the spall time record at ± 30 seconds (i.e. the spike could be due to the removal of concrete material at spalling which exposes the sensor to direct heating). Generally, however, no discernable temperature behavior was recorded that indicated a prediction metric for the occurrence of explosive thermal spall.

Figure 11 through Figure 18 show that temperature and axial stress do not show a direct driving relationship to thermal spalling. Additionally, the directly measured concrete mix properties determined for this dataset were not found to present a singular predictor of thermal spalling behavior. Pore pressure has been shown to not be a direct driving force for concrete thermal spalling behavior [44] with additional papers stating there is no direction relationship between pore pressure and thermal spalling behavior [44,45], however these claims have been refuted by Kodur and Banerji (2021) [43]. The literature record in conjunction with the experimental results herein show that a combination of mechanical, thermal, and pore pressures contribute to the phenomena of thermally-induced explosive concrete spalling, suggesting that a confluence of several contributing factors is necessary to predict thermal spall behaviors.

4.4 Effects of Varying Heat Flux at Similar Axial Load

Figure 19 repeats Figure 13 (b) and Figure 12 (b) with the inclusion of two C3 specimens at a lower heat flux exposure (derived from increasing the standoff between the burner and concrete panel specimen surface). In Figure 19 (a) we see that the temperature profile for the lower heat flux application is indistinguishable from the higher flux cases at the 25.4 mm (1 in) depth thermocouple. The behavior of temperature at this depth is an indication of the peak allowable thermal transfer, or energy absorption, of similar normal weight concrete mixes. The thermal behavior seen in the temperature time history presented in Figure 13 and duplicated in Figure 19 with the lower heat flux inclusion suggest a peak transfer which is supported by current concrete thermal transfer theory for structural thickness with good agreement between experimental evaluations and simplified temperature estimate equations like Wickström's Equation [46]. Reviewing Figure 19 (b) we see that the MC and VD of the two lower flux C3 panel specimens would be expected not to spall, however the thermal load appears to shift the cubic spalled specimen regression -99% confidence interval boundary downward. There may exist a threshold surface defined by MC, VD, and heat flux in three dimensions. However, an additional study

focused on heat flux variation is required to address the change in spalling behavior to evaluate the existence of a threshold surface, as well as to evaluate the risk of spalling for normal weight concrete with regard to the thermal load. The initial apparatus setup thermal testing calibrations, completed before the initiation of the dataset presented in this paper, suggested a minimum required heat flux to generate the spalling condition.

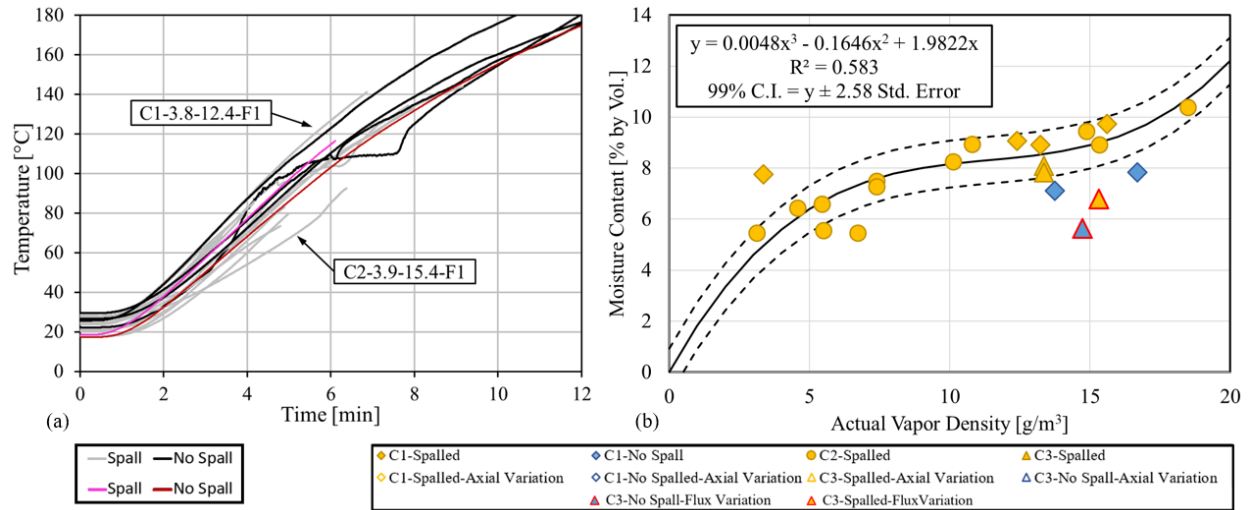


Figure 19: Heat Flux Variation (a) 25.4 mm depth temperature time history (b) MC to VD

CHAPTER 5 – SUMMARY AND CONCLUSIONS

This paper presents the successful application of the experimental apparatus initially outlined by Maluk et al. (2016) to observed thermally-induced concrete spall behavior under repeatable conditions. The paper attempts to address the lack of concrete material description in the current thermally-induced explosive concrete spall behavior literature, most notably detailed description of the day-of-testing pre-heat exposure moisture state for both liquid and vapor states. Special emphasis is placed on the use of actual vapor density, VD, to be used instead of the relatively humidity, RH, percentage. The results presented in this paper are, currently, non-conclusive for the prediction of thermally induced explosive concrete spall behavior, however the intent is to outline methods for the detailed description of concrete mix and day-of-testing moisture state to aid future analysis and prediction efforts as a validation dataset. The items listed below are of note and summarize the main findings.

- Internal temperature time history over the heat exposure, initial state MC, initial state VD (or RH and ambient material temperature), and axial load as presented herein, was not found to be sufficient to predict spall behavior; neither time to spall or spall occurrence. These findings, and the reference literature provided herein, indicate/suggest pore pressure as an important contributor, if not, a controlling element for predicting thermally induced explosive concrete spall. However, accurate moisture condition and void structure, including permeability, definition are principal to accurately account for and predict pore pressures [47].
- Axial load was found to contribute to spall behavior with limited axial load resulting in minimal or no spalling, while typical service level axial loading resulted in spall depths on the order of 3 times that of the limited axial load case. The typical specimen was subjected to an axial load of 14-18% of the specimen's nominal compressive strength, as a generic representation of in-service stress. For a pair of C1 and C3 panels with similar moisture conditions, the axial load level was doubled or nearly eliminated to observe the impact of increased or reduced mechanical stress on the occurrence of heat-induced explosive spall. This finding may suggest that experimentation lacking mechanical loading stress (i.e. non-thermal stresses) may under report spalling behavior, significantly.
- Actual vapor density appears to be a better descriptor than relative humidity percentage when defining the initial concrete moisture condition. As discussed in the results concerning Figure 12, specimens may exhibit the same moisture content and relative humidity percentages, but do not have the same actual vapor density. The inclusion of moisture content, relative humidity, and ambient material temperature or the moisture content and actual vapor density should be included in future work regarding the prediction of thermally induced explosive concrete spall behavior.
- Spall behavior exhibited in this experimental dataset are in disagreement with the moisture content percentage thresholds defined by Hertz and Eurocode 2 and 4 [18,39,40]. Spalling was observed at moisture content percentage well below the Hertz defined threshold, between 3 and 4%, while three specimens exhibited spalling below the Eurocode specified 2.5% threshold. Additional research may be warranted to explore the existence of a threshold, however the limited data available in this test suggest the threshold may be better described by

a function which includes both moisture content percentage and actual vapor density as discussed and shown in Figure 12.

- Although curing process has been shown to alter the permeability of concrete [22], the curing method did not present any discernable difference in thermally-induced explosive concrete spall behavior in this dataset.

REFERENCES

- [1] M. Abrams, *Compressive Strength of Concrete at Temperatures to 1600F*, Portland Cement Association, Skokie, USA, 1971.
- [2] G.T.G. Mohamedbhai, Effect of exposure time and rates of heating and cooling on residual strength of heated concrete, *Mag. Concr. Res.* 38 (1986) 151–158. <https://doi.org/10.1680/mac.1986.38.136.151>.
- [3] M. Husem, The effects of high temperature on compressive and flexural strengths of ordinary and high-performance concrete, *Fire Saf. J.* 41 (2006) 155–163. <https://doi.org/10.1016/j.firesaf.2005.12.002>.
- [4] Q. Ma, R. Guo, Z. Zhao, Z. Lin, K. He, Mechanical properties of concrete at high temperature—A review, *Constr. Build. Mater.* 93 (2015) 371–383. <https://doi.org/10.1016/j.conbuildmat.2015.05.131>.
- [5] ACI, *Code requirements for determining fire resistance of concrete and masonry construction assemblies*, American Concrete Institute, Farmington Hills, MI, 2014.
- [6] F. Bai, Q. Guo, K. Root, C. Naito, S. Quiel, Blast Vulnerability Assessment of Road Tunnels with Reinforced Concrete Liners, *Transp. Res. Rec.* 2672 (2018) 156–164.
- [7] J.-C. Mindeguia, P. Pimienta, A. Noumowé, M. Kanema, Temperature, pore pressure and mass variation of concrete subjected to high temperature — Experimental and numerical discussion on spalling risk, *Cem. Concr. Res.* 40 (2010) 477–487. <https://doi.org/10.1016/j.cemconres.2009.10.011>.
- [8] L.T. Phan, J.R. Lawson, F.L. Davis, Effects of elevated temperature exposure on heating characteristics, spalling, and residual properties of high performance concrete, *Mater. Struct.* 34 (2001).
- [9] A. Noumowe, H. Carre, A. Daoud, H. Toutanji, High-Strength Self-Compacting Concrete Exposed to Fire Test, *Jounal Mater. Civ. Eng.* 18 (2006) 754–758. [https://doi.org/10.1061/\(ASCE\)0899-1561\(2006\)18:6\(754\)](https://doi.org/10.1061/(ASCE)0899-1561(2006)18:6(754)).
- [10] Rail Accident Investigation Branch, *Technical Investigation Report concerning the Fire on Eurotunnel Freight Shuttle 7412 on 11 September 2008*, Department for Transport, Channel Tunnel, 2010. http://www.railwaysarchive.co.uk/documents/RAIB_ChannelTunnel2008.pdf (accessed July 10, 2020).
- [11] A.Y. Elghazouli, K.A. Cashell, B.A. Izzuddin, Experimental evaluation of the mechanical properties of steel reinforcement at elevated temperature, *Fire Saf. J.* 44 (2009) 909–919. <https://doi.org/10.1016/j.firesaf.2009.05.004>.
- [12] S. Quiel, C. Irwin, C. Naito, N. Vermaak, Mechanical Characterization of Normal and High-Strength Steel Bars in Reinforced Concrete Members under Fire, *J. Struct. Eng.* 146 (2020). [https://doi.org/10.1061/\(ASCE\)ST.1943-541X.0002644](https://doi.org/10.1061/(ASCE)ST.1943-541X.0002644).
- [13] C. Maluk, L. Bisby, M. Krajcovic, J.L. Torero, A Heat-Transfer Rate Inducing System (H-TRIS) Test Method, *Fire Saf. J.* (2016). <https://doi.org/10.1016/j.firesaf.2016.05.001>.
- [14] G. Choe, G. Kim, M. Yoon, E. Hwang, J. Nam, N. Guncunski, Effect of moisture migration and water vapor pressure build-up with the heating rate on concrete spalling type, *Cem. Concr. Res.* 116 (2019) 1–10. <https://doi.org/10.1016/j.cemconres.2018.10.021>.
- [15] D. Gawin, F. Pesavento, B.A. Schrefler, Towards prediction of the thermal spalling risk through a multi-phase porous media model of concrete, *Comput. Methods Appl. Mech. Eng.* 195 (2006) 5707–5729.
- [16] U. Wickström, *Temperature Calculation in Fire Safety Engineering*, Springer International Publishing, Cham, 2016. <https://doi.org/10.1007/978-3-319-30172-3>.

- [17] K.-H. Kim, S.-E. Jeon, J.-K. Kim, S. Yang, An experimental study on thermal conductivity of concrete, *Cem. Concr. Res.* 33 (2003) 363–371. [https://doi.org/10.1016/S0008-8846\(02\)00965-1](https://doi.org/10.1016/S0008-8846(02)00965-1).
- [18] CEN, EN 1992-1-2: Eurocode 2: Design of concrete structures - Part 1-2: General rules - Structural fire design, European Commission for Standardization, Brussels, Belgium, 2008.
- [19] D.-W. Ryu, J.-W. Ko, T. Noguchi, Effects of simulated environmental conditions on the internal relative humidity and relative moisture content distribution of exposed concrete, *Cem. Concr. Compos.* 33 (2011) 142–153. <https://doi.org/10.1016/j.cemconcomp.2010.09.009>.
- [20] T.Z. Harmathy, Effect of moisture on the fire endurance of building elements, *Moisture Mater. Relat. Fire Tests*. American Society for Testing and Materials-Special Technical Publication No. 385 (1965) 74–95. <https://doi.org/978-0-8031-5970-9>.
- [21] G.W. Shorter, T.Z. Harmathy, Discussion on the fire resistance of prestressed concrete beams, *Proc. Inst. Civ. Eng.* 20 (1961) 313–315.
- [22] M.V. Villar, P.L. Martin, F.J. Romero, V. Gutierrez-Rodrigo, J.M. Barcala, Gas and Water Permeability of Concrete, *Centro de Investigaciones Energeticas Medioambientales y tecnologicas*, 2012. <https://www.osti.gov/etdeweb/servlets/purl/22006614>.
- [23] J. Jiang, Y. Yuan, Relationship of moisture content with temperature and relative humidity in concrete, *Mag. Concr. Res.* 65 (2013) 685–692. <https://doi.org/10.1680/mac.12.00190>.
- [24] P. Kalifa, F.-D. Menneteau, D. Quenard, Spalling and pore pressure in HPC at high temperatures, *Cem. Concr. Res.* 30 (2000) 1915–1927. [https://doi.org/10.1016/S0008-8846\(00\)00384-7](https://doi.org/10.1016/S0008-8846(00)00384-7).
- [25] ASTM International, ASTM C642 Standard Test Method for Density, Absorption, and Voids in Hardened Concrete, 2013. <https://doi.org/10.1520/C0642-13>.
- [26] ASTM International, ASTM C1757 Standard Test Method for Determination of One-Point, Bulk Water Sorption of Dried Concrete, 2013. <https://doi.org/10.1520/C1757-13>.
- [27] P. Kalifa, G. Chéné, C. Gallé, High-temperature behaviour of HPC with polypropylene fibres: From spalling to microstructure, *Cem. Concr. Res.* 31 (2001) 1487–1499. [https://doi.org/10.1016/S0008-8846\(01\)00596-8](https://doi.org/10.1016/S0008-8846(01)00596-8).
- [28] T. Hulin, C. Maluk, L. Bisby, K. Hodicky, J.W. Schmidt, H. Stang, Experimental Studies on the Fire Behaviour of High Performance Concrete Thin Plates, *Fire Technol.* 52 (2016) 683–705. <https://doi.org/10.1007/s10694-015-0486-x>.
- [29] I. Hager, K. Mróz, Role of Polypropylene Fibres in Concrete Spalling Risk Mitigation in Fire and Test Methods of Fibres Effectiveness Evaluation, *Materials.* 12 (2019) 3869. <https://doi.org/10.3390/ma12233869>.
- [30] F. Lu, On the prediction of concrete spalling under fire, ETH Zurich, 2015. <https://doi.org/10.3929/ethz-a-010581905>.
- [31] D. Gawin, F. Pesavento, B. Schrefler, Hygro-thermo-chemo-mechanical modelling of concrete at early ages and beyond. Part I: Hydration and hygro-thermal phenomena, *Int. J. Numer. Methods Eng.* 67 (2006) 299–331. <https://doi.org/10.1002/nme.1615>.
- [32] Y. Ichikawa, Prediction of Pore Pressures, Heat and Moisture Transfer Leading to Spalling of Concrete during Fire, Doctoral Thesis, University of London, 2000.
- [33] ASTM International, ASTM C39 Standard Test Method for Compressive Strength of Cylindrical Concrete Specimens, 2015. <https://doi.org/10.1520/C0039>.

- [34] ASTM International, ASTM C469 Standard Test Method for Static Modulus of Elasticity and Poisson's Ratio of Concrete in Compression, 2014. https://doi.org/10.1520/C0469_C0469M-14.
- [35] ASTM International, ASTM C496 Standard Test Method for Splitting Tensile Strength of Cylindrical Concrete Specimens, 2011. <https://doi.org/10.1520/C0496>.
- [36] ASTM International, ASTM F2170 Standard Test Method for Determining Relative Humidity in Concrete Floor Slabs Using in situ Probes, 2019. <https://doi.org/10.1520/F2170-19A>.
- [37] International Association for the Properties of Water and Steam, Revised Release on the Pressure along the Melting and Sublimation Curves of Ordinary Water Substance, 2011. <http://www.iapws.org/relguide/MeltSub2011.pdf>.
- [38] ASTM, Test Methods for Determining Effects of Large Hydrocarbon Pool Fires on Structural Members and Assemblies, ASTM International, West Conshohocken, PA, 2016.
- [39] K.D. Hertz, Limits of spalling of fire-exposed concrete, *Fire Saf. J.* 38 (2003) 103–116. [https://doi.org/10.1016/S0379-7112\(02\)00051-6](https://doi.org/10.1016/S0379-7112(02)00051-6).
- [40] B. EN, Eurocode 4: Design of composite steel and concrete structures - Part 1-1: General rules and rules for buildings, Lond. Br. Stand. Inst. (2004).
- [41] J.C. Mindeguia, P. Pimienta, I. Hager, H. Carre, Influence of water content on gas pore pressure in concretes at high temperature, in: Delft, the Netherlands, 2011: pp. 113–121.
- [42] N.B. Hutcheon, G.O. Handegord, *Building Science for a Cold Climate*, Wiley, Toronto, 1984.
- [43] V.K.R. Kodur, s. Banerji, Modeling the fire-induced spalling in concrete structures incorporating hydro-thermo-mechanical stresses, *Cem. Concr. Compos.* 117 (2021). <https://doi.org/10.1016/j.cemconcomp.2020.103902>.
- [44] R. Jansson, L. Boström, The Influence of Pressure in the Pore System on Fire Spalling of Concrete, *Fire Technol.* 46 (2010) 217–230. <https://doi.org/10.1007/s10694-009-0093-9>.
- [45] J.C. Mindeguia, P. Pimienta, H. Carre, C. La Borderie, Experimental study on the contribution of pore vapour pressure to the thermal instability risk of concrete spalling due to fire exposure, Centre Scientifique et Technique du Batiment - Universite Paris, 2009. https://d1wqtxts1xzle7.cloudfront.net/41979856/Experimental_study_on_the_contribution_o20160203-30232-hlzt9v.pdf?1454534348=&response-content-disposition=inline%3B+filename%3DExperimental_study_on_the_contribution_o.pdf&Expires=1603048689&Signature=Igo~yZ04tUGvRFgOE1BU~Lwcn7DZNL-WGxJCx7kIV2oqXZNXn~bgle3h6B5J1P7Ff3AVl36lvDvXpRLX~n4cNs56yJVVtWl~I~~rLAVwBXCq-LA18MWF7g0FMf~qQLR9xNeufbftXPUC7BHQ2Pvm2YQ4Va3ok-YvRvCllcEo2vO4j4MzOZAAPlqPjjbM~AlCwr bx-kuAF2OU5nskNGftws0gv8TyxSnD-S0Tq92oZ0XgtJD-pAVkTWsjek~BgmVSCgIVTY21X7dvYHfZhidJCY17hn7B4eD1PXAEKcyXp1ISM4jK6v9RdCTMTmZMf6OYKaCzefxc2sqUrYMMwkYjg__&Key-Pair-Id=APKAJLOHF5GGSLRBV4ZA.
- [46] A. Buchanan, A. Abu, Structural design for fire safety, 2017. <https://books.google.com/books?hl=en&lr=&id=o7fBDQAAQBAJ&oi=fnd&pg=PA15&dq=structural+design+for+fire+safety+buchanan&ots=KLSsOSKDAb&sig=IG-AvQwNLvukz-BBCDI3NEH55-E> (accessed August 15, 2017).
- [47] Z.P. Bazant, W. Thonguthai, Pore pressure in heated concrete walls: theoretical prediction, *Mag. Concr. Res.* 31 (1979) 67–76.

APPENDIX A – TECHNOLOGY TRANSFER ACTIVITIES

1 Accomplishments

- Established and refined the experimental apparatus setup and testing procedure over 60 concrete samples.
- Recorded and analyzed 24 specimens for spalling behavior.
- Submitted 1 peer reviewed journal publication

1.1 What was done? What was learned?

- Fabricated 60 concrete specimens for testing in the experimental apparatus
- Submitted 1 peer reviewed journal publication

1.2 How have the results been disseminated?

- The work was presented at two workshop/lecture presentations
- The work was refined for peer review journal publication and is awaiting review
- The work in total is reported herein for public availability

2 Participants and Collaborating Organizations

Name: Aerik Carlton

Location: Lehigh University, Bethlehem, Pennsylvania

Contribution: Researcher and PhD student

Name: Ziyan Ouyang

Location: Lehigh University, Bethlehem, Pennsylvania

Contribution: Researcher, MS student, and current PhD student

Name: Spencer Quiel, PhD

Location: Lehigh University, Bethlehem, Pennsylvania

Contribution: Principle Investigator

Name: Clay Naito, PhD

Location: Lehigh University, Bethlehem, Pennsylvania

Contribution: Principle Investigator

Names: Kyle Root*, Isabella Romano, Quinton Ritchie, Amanda Korwek, Spencer Levenson

Location: Lehigh University, Bethlehem, Pennsylvania

Contribution: Research Assistance, MS* and undergraduate students

3 Outputs

Journal publications

Submitted to Fire Safety Journal

Presentations

ADSC, The International Association of Foundation Drilling, Fall Meeting: Outreach Education, “Experimental Investigation of the Relationship between Concrete Spalling under Heat Exposure and Concrete Moisture Content.” November 21, 2019.

Workshops

UTC-UTI, University Transportation Center for Underground Transportation Infrastructure, Colorado School of Mines, “Experimental Investigation of the Relationship between Concrete Spalling under Heat Exposure and Concrete Moisture Content.” October 18, 2019.

4 Outcomes

The experimental testing considering single sided heating of hydrocarbon fire intensity was completed on structural sized concrete elements under typical in-service loading to allow for computation analysis for the prediction of thermally-induced concrete spalling behavior indicative of a concrete tunnel liner experiencing vehicular fire. The experimentation was used as an opportunity to exposure undergraduate students to the research process, and the information is being disseminated via presentations and publication. The work yields a base-line for spall prediction in the context of roadway tunnel, and subsequent work will provide computational prediction of the behavior to inform structural design, reliability, and probabilistic life-cycle costs associated with vehicular fire hazards in tunnels. Additionally, a codified moisture content threshold for thermally induced spalling behavior was disproved.

APPENDIX B - DATA FROM THE PROJECT

Table 7 shows a brief selection from one worksheet of the accompanying raw experimental data Excel file. For the 24 experimental specimens included in this report 21 raw data files were included, as several tests had corrupted full time-history files and were therefore unable to be included. The test specimen label is in the first cell, followed by 9 to 10 columns (C3 specimens included an extra embedded thermocouple sensor).

- Column 1 shows the Timestamp of the test including the date and time
- Column 2 shows the record number, records were sampled twice per second
- Column 3 and 4 shows the right and left load cell output in kips (1 kip = 1000 lbs = 4.4482 kN)
- Column 5 to 9 or 10 shows the temperatures in degrees Celsius: T_1, T_3, and T_5 are the embedded thermocouple sensors at 1, 3, and 5 inches from the heated specimen face for Concrete 1 and 2; while T0, T025, T05, T10 are the embedded thermocouple sensors at 0, 0.25, 0.5, and 1.0 inches from the heated specimen face for Concrete 3; T0_top and T0_bot are surface placed thermocouple sensors in contact with the heated surface of the concrete specimen.

Table 7: Example Selection from the Accompanying Excel File of Raw Experimental Data

C1-4.1-15.6-F1								
TOA5	1704	CR1000X	1704	CR1000X.Std.01		CPU:PANEL.CR1X		58631
TIMESTAMP	RECORD	R_LC	L_LC	T_1	T_3	T_5	T0_top	T0_bot
TS	RN	kip	kip	Deg C	Deg C	Deg C	Deg C	Deg C
		Smp	Smp	Smp	Smp	Smp	Smp	Smp
7/12/2019 8:46	0	47.13	43.98	26.51	26.49	26.60	26.64	26.75
46:17.5	1	47.13	43.98	26.51	26.50	26.61	26.65	26.76
7/12/2019 8:46	2	47.13	43.98	26.51	26.50	26.61	26.65	26.75
46:18.5	3	47.13	43.98	26.51	26.50	26.61	26.65	26.76
7/12/2019 8:46	4	47.13	43.98	26.51	26.50	26.61	26.63	26.76
...

Note: the surface placed thermocouple sensors experienced movement during heat exposure due to being sandwiched between the spall debris protection screen and the concrete specimen. Exact location on the face was difficult to duplicate between tests for these sensors. The surface sensors would move as the spall debris screen expanded during heating, were subject to vapor release from the concrete, and at times would be covered with spalled material. The value in the surface sensors, however, is allowing for heat exposure start and stop and spall time to be estimated.